ARTICLE

Host factor TIMP1 sustains long-lasting myeloid-biased hematopoiesis after severe infection

Tengfei Song[1], Yonghong Yao[1], Julien Papoin[1], Barbara Sherry[1,2], Betty Diamond[1,2], Hua Gu[3], Lionel Blanc[1,2], and Yong-Rui Zou[1]

Infection is able to promote innate immunity by enhancing a long-term myeloid output even after the inciting infectious agent has been cleared. However, the mechanisms underlying such a regulation are not fully understood. Using a mouse polymicrobial peritonitis (sepsis) model, we show that severe infection leads to increased, sustained myelopoiesis after the infection is resolved. In post-infection mice, the tissue inhibitor of metalloproteinases 1 (TIMP1) is constitutively upregulated. TIMP1 antagonizes the function of ADAM10, an essential cleavage enzyme for the activation of the Notch signaling pathway, which suppresses myelopoiesis. While TIMP1 is dispensable for myelopoiesis under the steady state, increased TIMP1 enhances myelopoiesis after infection. Thus, our data establish TIMP1 as a molecular reporter of past infection in the host, sustaining hyper myelopoiesis and serving as a potential therapeutic target for modulating HSPC cell fate.

Introduction

Immunity against pathogens relies on lymphoid and myeloid cells, which are maintained in a balanced ratio under a steady state through a stepwise developmental process from hematopoietic stem cells (HSCs) and multipotent progenitor (MPP) cells to the downstream lymphoid or myeloid lineage–committed progenitor cells (Pietras et al., 2015; Rodriguez-Fraticelli et al., 2018). The lymphoid/myeloid equilibrium, however, can be precipitously disrupted by systemic bacterial or viral infection. Upon sensing the pathogen-associated molecular patterns (PAMPs) and stimulated by proinflammatory cytokines, quiescent HSCs are activated and hyperproliferative HSCs preferentially differentiate toward the myeloid lineage cells to meet the increased demand for innate immune defense during acute infection (Trumpp et al., 2010; Baldridge et al., 2011; Takizawa et al., 2012; Chavakis et al., 2019; Hormaechea-Agulla et al., 2020; Caiado et al., 2021). Such an emergency myelopoiesis is considered transitory since PAMPs are eliminated after pathogen clearance and proinflammatory cytokines decrease to basal levels when the body returns to the normal and healthy state. However, in some cases, enhanced myelopoiesis persists in the absence of inciting infectious agents and the known inflammatory mediators after the resolution of infection (Kaufmann et al., 2018). While a persistently high output of myeloid cells following infection could improve innate immunity (Ciarlo et al., 2020; Moorlag et al., 2020), enhanced myelopoiesis is often associated with chronic inflammatory conditions, such as autoimmune diseases, cancer, and "inflammaging" (Caiado et al., 2021; Niu et al., 2013; Pang et al., 2011; Schultze et al., 2019; Sudo et al., 2000). Thus, to modulate innate immunity and control the harmful side effects of inflammation, it is important to understand whether infection-experienced animals manage the long-term enhanced myelopoiesis by altering the HSC intrinsic differentiation program or the bone marrow (BM) hematopoietic niche microenvironment that controls the fate decision during HSC differentiation.

Hematopoietic stem and progenitor cells (HSPCs) reside in the BM in a specialized niche that is comprised of multiple populations of cells, including adipocytes, endothelial cells, fibroblasts, osteoblasts, and other mesenchymal stromal cells (Baccin et al., 2020; Baryawno et al., 2019; Morrison and Scadden, 2014; Tikhonova et al., 2019). These cells provide structural integrity, cellular communication, and local instructive signals to maintain HSC quiescence and self-renewal, as well as to regulate HSPC differentiation. Infection induces a variety of damages to the BM hematopoietic niche (Batsivari et al., 2020). For instance, sepsis can lead to the ablation of IL-7–producing osteoblasts that support lymphopoiesis (Terashima et al., 2016) and causes endothelial malfunction (Maneta et al., 2023). The sepsis-caused damage to other cellular components of the BM niche has not been well determined. It is also unclear

whether sepsis-injured BM niche can be fully restored and to what extent it affects the myeloid/lymphoid lineage balance after severe infection.

Here, we explored the long-term impact of severe infection on HSCs per se, as well as on the hematopoietic microenvironment in mice surviving polymicrobial peritonitis (sepsis). We observed a persistent increase in myelopoiesis in mice, even months after the initial infection had resolved. We demonstrate that the tissue inhibitor of metalloproteinases 1 (TIMP1) is constitutively upregulated in the infection-experienced mice, which facilitates HSPCs to adopt a myeloid-biased differentiation program. Such a regulation is dependent on the TIMP1-mediated inhibition of Notch signaling in HSPCs.

Results

Increased myelopoiesis persists in mice surviving severe infection

B6 mice subjected to cecal ligation and puncture (CL&P) developed polymicrobial peritonitis, bacteremia, septic shock, multiorgan dysfunction (Cuenca et al., 2010; Fink, 2014), and ~50% of treated mice became moribund under our surgical procedure (Fig. S1 A). The hematopoietic system is severely damaged in septic mice, as lymphopenia and emergency myelopoiesis develop within days following CL&P surgery (Hotchkiss et al., 2013; van der Poll et al., 2021; Wichterman et al., 1980). Thus, to investigate whether the generation of lymphoid and myeloid cells in mice surviving severe infection could be restored to the preinfection balanced state, we decided to use mice surviving CL&P surgery as our model. We examined lymphoid and myeloid cells in the peripheral lymphoid organs of CL&P and sham-treated mice at different time points after surgery. We found that splenic B cell counts normalized 2 wk after CL&P surgery (Fig. S1 B), consistent with a previous report (Terashima et al., 2016). T cell numbers in CL&P mice recovered at a slower rate relative to B cells, with a complete normalization 10 wk after surgery (Fig. S1 C). In contrast to lymphoid cells, the counts of peripheral monocytes and granulocytes remained higher in CL&P mice than in controls 12 wk after surgery (Fig. S1 D), and there was an increase in circulating myeloid cells even 7 mo after CL&P surgery (Fig. S1 E). Given the relatively short lifespan of peripheral myeloid cells, it is likely that infection has altered the BM myeloid output.

To determine whether the increase in the peripheral myeloid cells was due to an enhanced BM myelopoiesis, we analyzed the BM compartment in mice surviving sepsis. The BM of CL&P mice had higher cellularity compared to sham mice, with a similar number of B cells but approximately a twofold higher count of monocytes ($CD11b^+Ly6C^+$) and granulocytes ($Ly6G^+$) (Fig. 1 A). There was also a 1.8-fold increase in the number of HSPCs (LSK: Lineage marker $[Lin]^-$ c-Kit$^+$ Sca-1$^+$) in the BM of CL&P mice relative to sham mice (Fig. 1 B). Within the LSK population, lymphoid-primed MPP4 cells and myeloid-biased MPP2 and MPP3 cells, as well as long-term (LT-) and short-term (ST-) HSCs can be identified using CD150, CD48, Flt3, and CD34 (Fig. S1 F). We found a comparable number of MPP4 cells in sham and CL&P mice, however, the number of MPP2 and

MPP3 cells was increased 4.6- and 3.6-fold respectively in CL&P mice over sham mice (Fig. 1 B). Overall, the increased LSK cells in CL&P mice contained higher proportions of MPP2 and MPP3 subsets and decreased MPP4 and ST-HSCs, whereas the percentage of LT-HSCs remained unchanged in the CL&P BM compared with control mice (Fig. 1 C). Thus, the cellular expansion of MPP3 cells resulted in a drastically biased ratio of MPP3 to MPP4 cells in the BM of CL&P mice compared with sham mice (Fig. 1 D). Collectively, these data highlight a different impact of severe systemic infection on the production of lymphoid and myeloid cells, with lymphopoiesis only transiently impaired in the septic phase, whereas the myelopoiesis is continuously augmented during septic shock and after infection has resolved.

HSPC differentiation program is altered in mice surviving severe infection

To understand the mechanisms underlying the myeloid-biased HSPC differentiation in mice surviving severe infection, we performed single-cell RNA sequencing (scRNA-seq) on LSK cells sorted from the BM of mice at week 12 after sham or CL&P surgery (Fig. S2, A and B). After quality control and exclusion of contaminating cells expressing lineage-restricted genes (Table S1), a dataset containing 3,021 and 3,843 LSK cells respectively of sham and CL&P mice was processed to generate graph-based clusters using the smart local moving (SLM) algorithm (Fig. S2 C). Based on the top differentially expressed genes (DEGs) representing signature genes for HSCs and MPPs, we conducted a reference-based classification using published datasets to annotate the seven unsupervised clusters as five distinct cell states (Fig. 2 A; Fig. S2, D and E; and Table S2). The cluster identity was further validated as UMAP plots displayed nearly identical gene expression profiles between the top features of annotated clusters and the published signature genes of HSC and MPP subsets (Fig. S2, E and F) (Klein et al., 2022). Cell-type proportion analysis of the scRNA-seq data revealed an expansion of MPP2 and MPP3 cells and a decrease in MPP4 cells in the CL&P sample (Fig. 2 B), consistent with the flow cytometry results (Fig. 1 C).

Next, we conducted trajectory analyses to infer cell-fate specification and differentiation of HSPCs after infection. We designated cells expressing signature genes of dormant LT-HSCs (e.g., *Cdkn1c, Tcf15, Neo1, Pdzk1ip1, Fgfr1, Mmrn1,* and *Tinagl1*) as the starting cell state (the root node 0) and used Monocle 3 to build a trajectory tree, which identified three branch points leading to five trajectory outcomes (leaf nodes 1–5) over pseudotime (Fig. 2 C). By comparing the pseudotime-highlighted trajectory plot to the cell state-highlighted one, we observed that HSCs were enriched in leaf node 1, which was closest to the root, whereas MPP2, MPP3, and MPP4 diverged from three branch points and were distributed over the remainder of the trajectories, and cycling cells were coalesced in leaf node 3 at the extremity of the trajectory tree (Fig. 2 C). Over pseudotime, cells progressively downregulated HSC markers (e.g., *Kit* and *Fgfr1*) along with an overall increase in the expression of genes associated with differentiation and the cell cycle (Fig. 2 D). To quantitatively assess cell state transition across the trajectory, we plotted cell states over pseudotime and calculated the frequencies of HSCs and
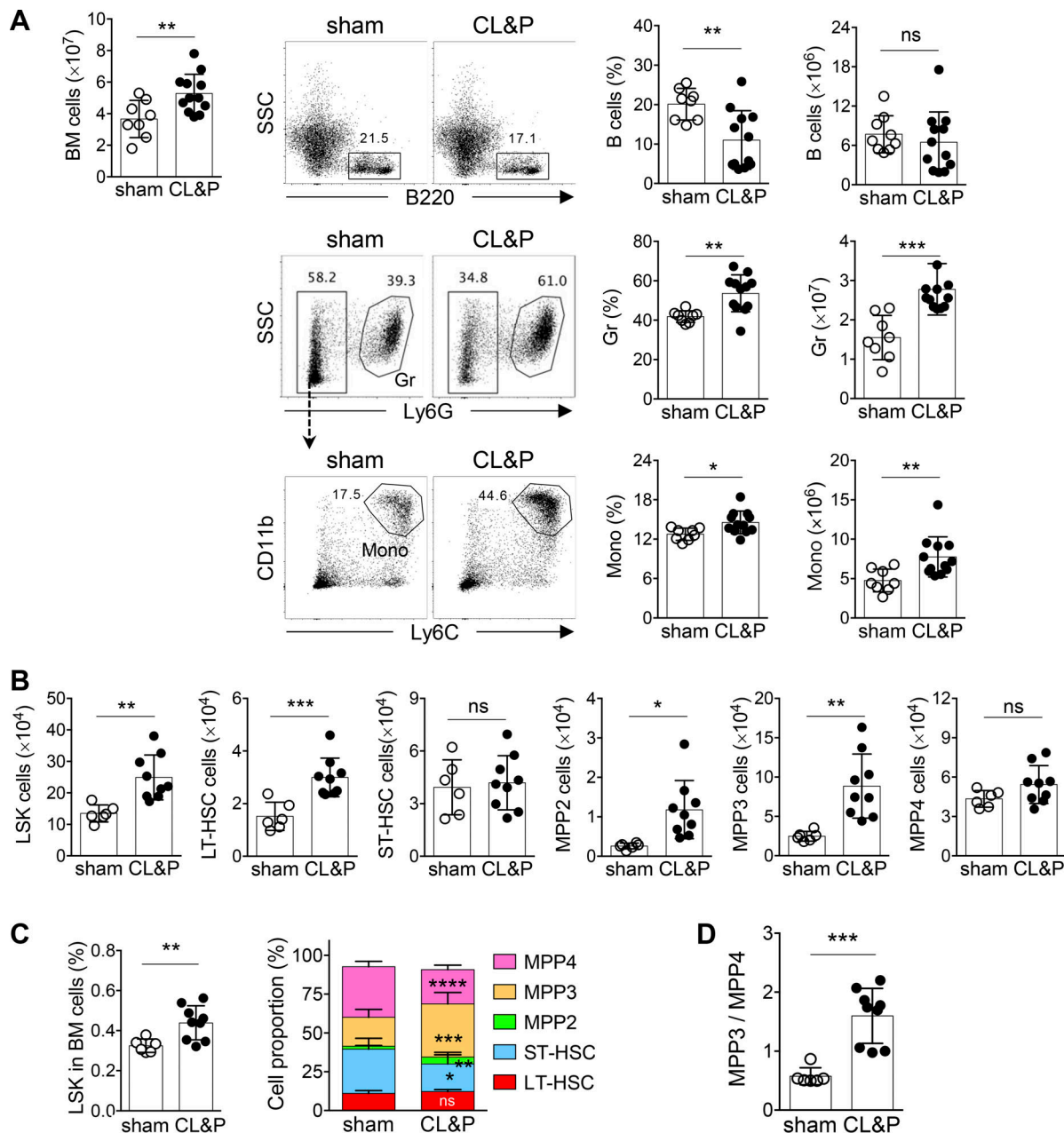
Figure 1. **Increased myeloid output in the BM of mice 12 wk after CL&P surgery. (A)** The top left graph shows the numbers of BM cells from two pairs of femurs and tibias of each mouse. The FACS plots and the middle panel of histograms show percentages of monocytes (Mono), granulocytes (Gr), and B cells. The right histogram panels show the statistics of the total numbers of monocytes, granulocytes, and B cells in two pairs of femurs and tibias per mouse. Data of sham ($n = 8$) and CL&P mice ($n = 12$) were generated from three independent experiments. Each dot represents an individual mouse and bars depict the average cell counts ± SD. ** $P < 0.01$; *** $P < 0.001$ (unpaired two-tailed Student's t test). **(B)** The absolute numbers of LSK, LT-HSCs, ST-HSCs, MPP2, MPP3, and MPP4 cells in sham and CL&P mice. Symbols show data of individual mice; bars show the mean value ± SD. * $P < 0.05$; ** $P < 0.01$; ns, $P > 0.05$. **(C)** Percentages of LSK cells are shown in the left panel. Proportions of HSC and MPP subsets within the LSK population are shown in the right histograms with stacked bars. Data are expressed as mean value ± SD. * $P < 0.05$; ** $P < 0.01$; *** $P < 0.001$; **** $P < 0.0001$; ns, $P > 0.05$. **(D)** The ratio of MPP3 to MPP4 cells. Symbols show data of individual mice; bars show the mean value ± SD. *** $P < 0.001$. **(B–D)** Data of six sham and nine CL&P mice were pooled from two independent experiments. P values by unpaired two-tailed Student's t test are indicated.

MPPs of sham or CL&P samples at each leaf node and between branch points (Fig. 2 E). We found an equivalent frequency of sham and CL&P HSCs in the root node (node 0). However, the frequency of CL&P HSCs in leaf node 1 was reduced to 60% of that in the sham control (Fig. 2 E), similar to the flow cytometry results demonstrating that the percentage of LT-HSC is unchanged while ST-HSC is proportionally decreased (Fig. 1 C). These data suggest defective self-renewal or accelerated cell cycle progression and differentiation of HSCs in CL&P mice. As expected, there was a drastic reduction in CL&P MPP4 frequency throughout the entire trajectory. Compared with sham MPP3 cells, half of which emerged in an earlier pseudotime
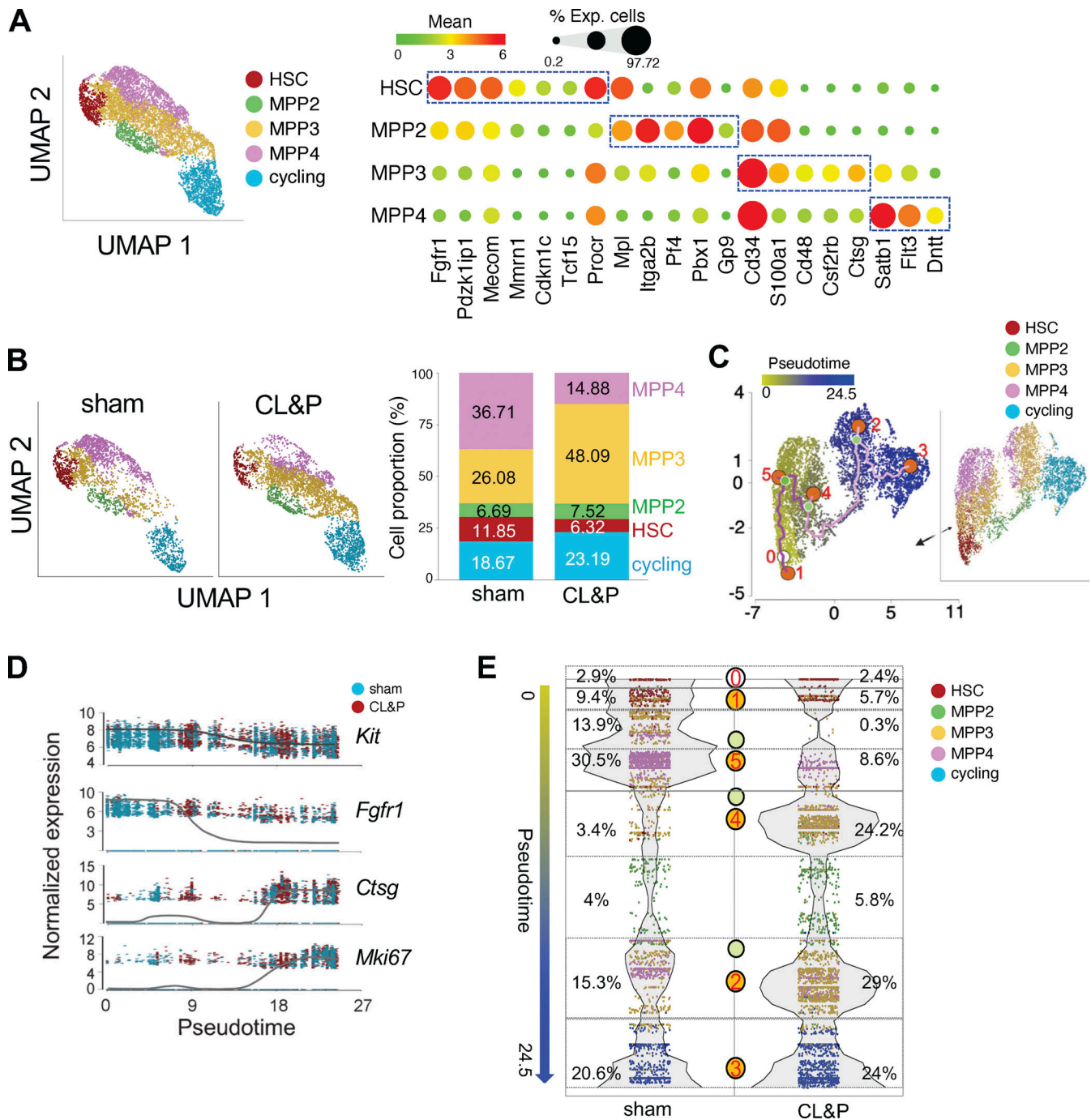
Figure 2. **scRNA-seq analysis of HSPC differentiation in mice surviving sepsis. (A)** LSK cells classified as clusters of different cell states are shown by a UMAP plot of merged sham and CL&P datasets (left). Dot plots show expression of the cell-state specific marker genes in the classified clusters (right). **(B)** Left UMAP plots show classified clusters in sham and CL&P datasets, respectively. Right panel displays proportions of cells in each cell state. **(C)** Branchpoint analysis for LSK cells of merged sham and CL&P datasets inferred by Monocle 3. LSK cell manifold was colored by the pseudotime value (left) or by the cell state (right). Root (0) and leaf nodes (1–5) are shown with numbers; branchpoints are represented by green dots. **(D)** Expression of selected genes correlated with pseudotime. Cells are colored by sham or CL&P samples. **(E)** Distribution of sham LSK cells or CL&P LSK cells in different cell states over pseudotime. Root (0) and leaf nodes (1–5) are shown with numbers; branchpoints are represented by green dots. Frequencies of cells in the indicated pseudotime domains are shown.

domain than MPP4 cells did, CL&P MPP3 differentiation occurred at later branch points and expanded at leaf nodes 2 and 4 (Fig. 2 E). The distinct topological positionings of MPP3 and MPP4 cells of sham and CL&P mice on the developmental

trajectories suggest that increased myelopoiesis in mice surviving severe infection is associated with altered differentiation programs at multiple cell-fate decision points during development.

HSPCs after infection are primed for proliferation with enhanced myeloid potential

To understand the biological and molecular underpinnings of the altered HSPC differentiation in mice surviving severe infection, we first identified genes that were differentially expressed in sham and CL&P LSK cells (Fig. S3 A) and then applied Gene Ontology (GO) analysis for genes that were up- or downregulated in CL&P LSK cells. We found that genes underrepresented in CL&P LSK cells included MHC molecules that were expressed by lymphoid-primed MPP4 cells (Fig. S3, A and C), whereas genes upregulated in CL&P LSK cells were associated with cellular biosynthesis and mitochondrial activities (Fig. S3 B). Gene set enrichment analysis (GSEA) complemented the results of GO analysis and showed that CL&P LSK cells were enriched for mitochondria biogenesis, tricarboxylic acid cycle, regulation of cell cycle transition and myeloid cell function (e.g., innate immune response) (Fig. 3 A). In contrast, sham LSK cells were enriched for autolysosome formation, somatic stem cell maintenance, and lymphocyte-mediated immunity (Fig. 3 A). In line with previous literature that high mitochondrial activity propels HSCs to exit dormancy (Chen et al., 2008; Nakamura-Ishizu et al., 2020; Vannini et al., 2016), we saw notable increases in pathways regulating the cell cycle in CL&P LSK cells (Fig. 3 A and Fig. S3 B). Consistent with these data, cell cycle profiling of sham and CL&P LSK cells with *Pcna* (expressed in all cell cycle phases except G0) and *Ccnb2* (expression level peaked in the G2/M phase) showed a decrease in the frequency of CL&P LSK cells in the G0 phases of the cell cycle compared with sham cells (Fig. S3, D and E). Flow cytometry analysis, which measured DNA content and the protein level of the cell proliferation marker Ki67, confirmed that there were indeed fewer quiescent CL&P LSK cells relative to sham cells (Fig. 3 B), with a notable reduction of LT-HSCs and MPP4 cells in the G0 phase in the CL&P BM (Fig. S3, F and G). This decrease in CL&P LSK cells in the G0 phase was correlated with an increased expression of the cell cycle activator *Cdk6* (Fig. S3 H). Expression of genes involved in the licensing of DNA replication, such as *Mcm3* and *Mcm5*, was particularly upregulated in CL&P LSK cells in the G0 phase. Conversely, *Foxo3*, known to regulate autophagy for maintaining HSC quiescence (Miyamoto et al., 2007), was expressed in fewer CL&P LSK cells and at a relatively lower level, and *Sirt7* that suppresses mitochondrial metabolism and myelopoiesis (Mohrin et al., 2015) was also downregulated in CL&P LSK cells in the G0 phase of the cell cycle compared to sham cells (Fig. S3 H). These analyses thus reveal that CL&P LSK cells are enriched for biological processes, distinct from those associated with quiescent sham LSK cells, and of note, preferentially use metabolic pathways that are known to facilitate myeloid differentiation (Ito et al., 2019).

Next, we interrogated lineage specification and fate decisions of sham and CL&P LSK cells. Principal component (PC) analysis showed that sham and CL&P LSK cells shared an overall similar distribution pattern, with HSCs high in PC1 scores, MPP4 cells high with PC2 scores, and MPP3 cells predominantly high in PC1 scores and low in PC2 scores (Fig. 3 C). Notably, a cluster of PC1^{low} PC2^{high} PC3^{high} cells expanded in the CL&P sample relative to sham control, and this cluster of cells predominantly resided in the leaf node 2 domain of the pseudotime rank (Fig. 3 D). We curated core signatures that specify each leaf node (Fig. S3, I and J; and Table S3) and profiled sham and CL&P LSK cells expressing leaf node 2 signature genes because the leaf node 2 core signature was likely associated with the aberrantly differentiated CL&P LSK cells. Compared with the expression profile of sham cells, CL&P cells singularly expressed a group of genes specific for granulocyte–monocyte progenitors (GMPs) that were developmentally downstream of LSK cells (Fig. 3 E). In particular, *Ms4a3*, a marker for GMPs committed to the myeloid lineage (Ishibashi et al., 2018; Liu et al., 2019), was aberrantly expressed in CL&P LSK cells, while its expression was barely detectable in sham LSK cells as previously reported (Fig. 3, E and F). To evaluate the lineage specification of *Ms4a3*-expressing CL&P LSK cells, we examined the expression of a lymphoid commitment marker, *Satb1*, in these cells (Satoh et al., 2013). We found that while *Satb1* expression was indeed restricted in sham MPP4 cells, it was expressed not only by CL&P MPP4 cells but also by the aberrant cluster of CL&P cells in the leaf node 2 domain (Fig. 3 F). As a matter of fact, a substantial amount of CL&P LSK cells co-expressed *Satb1* and *Ms4a3* (Fig. 3 G), as well as other myeloid and lymphoid-specific genes, such as *Ctsg* and *Dntt* (Fig. S3 K). These results reveal increased lineage plasticity of HSPCs in CL&P mice long after infection has resolved and suggest that a significant proportion of HSPCs that have begun lymphoid-lineage specification may eventually escape the lymphoid cell fate and develop into the myeloid lineage.

The hematopoietic microenvironment in sepsis-surviving mice sustains myeloid expansion

The above analyses show that HSPCs in mice surviving severe infection shifted from a quiescent to an active state, altered multiple biological processes, and adopted a myeloid-primed differential pathway. These functional changes could result from altered cell-autonomous developmental programs or be inflicted by infection-injured hematopoietic niche. To examine HSPC-intrinsic differentiation potential after infection, we transferred 2 × 10^6 BM cells from CD45.2$^+$ B6 mice 12 wk after sham or CL&P surgery into irradiated congenic CD45.1$^+$ B6.SJL mice, respectively. 6 wk after BM transplantation, CD45.2$^+$ BM cells from sham- or CL&P-treated mice generated an equivalent number of granulocytes and monocytes, as well as lymphocytes in the recipient mice (Fig. 4 A), demonstrating that the cell-intrinsic developmental potential of HSPCs from CL&P mice is normal. To determine whether the post-infection microenvironment influenced myeloid differentiation, we transferred 2 × 10^6 BM cells from naïve CD45.1$^+$ B6.SJL mice into irradiated B6 mice 12 wk after sham or CL&P surgery. 6 wk later, we found that CL&P recipients possessed significantly more myeloid cells relative to sham hosts whereas lymphocyte counts were comparable in both groups of hosts (Fig. 4 B). Since both sham and CL&P hosts received the same dose of irradiation, the effect of irradiation on the BM niche cannot account for the increased myeloid output in CL&P recipients. These results thus support that severe infection causes durable alterations in the host hematopoietic microenvironment that favor myelopoiesis.
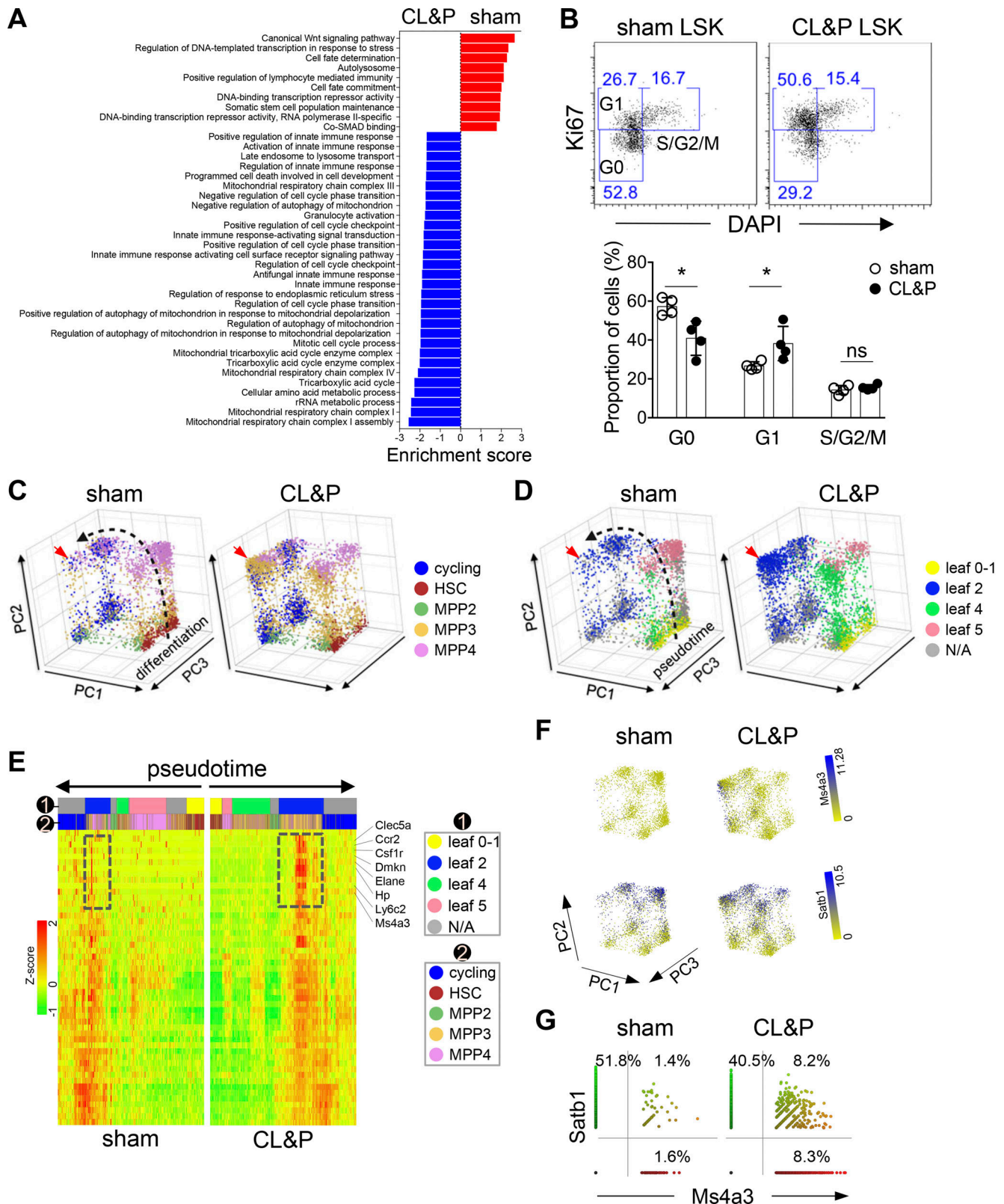
Figure 3. **HSPCs in mice surviving sepsis are active and acquire alternative myeloid differentiation potential. (A)** A waterfall plot shows biological processes and pathways enriched in sham LSK cells (red) and in CL&P LSK cells (blue). **(B)** Top FACS plots show cell cycle analysis of sham and CL&P LSK cells. Bottom panel shows statistical results with each dot representing data from an individual mouse (sham = 4, CL&P = 4; data from two independent experiments). Bars representing the mean value ± SD. * P < 0.05; ns, P > 0.05 (unpaired two-tailed Student's *t* test). **(C and D)** PCA for sham and CL&P LSK cells colored by the cell state (C), or by trajectory leaf nodes (D). Graphs are shown with logarithmic axes. Red arrows point to cells aberrantly expanded in the CL&P sample. **(E)** Heatmap of expression of the core signature genes of leaf node 2 (row) in sham and CL&P LSK cells (column) ordered by pseudotime. Annotations

by the leaf nodes (1) or by the cell states (2) are displayed at the top. Boxes in the heatmap highlight transcripts upregulated in CL&P LSK cells. **(F)** Projection of *Ms4a3* and *Satb1* expression on the PCA plots. **(G)** Scatterplots display co-expression of the lymphoid commitment gene *Satb1* and the myeloid commitment gene *Ms4a3* in LSK cells.

Based on our scRNA-seq data suggesting increased lineage plasticity of HSPCs in CL&P mice and the reciprocal transplantation results highlighting the host's impact on enhanced myelopoiesis, we hypothesized that the post-infection microenvironment redirects lymphoid precursors to the myeloid cell fate. To test this, we isolated lymphoid-primed MPP4 cells from naïve mice and examined their differentiation potential in sham or CL&P hosts. As previously reported, MPP4 cells primarily gave rise to B cells when transplanted into naive hosts, while MPP3 cells predominantly produced myeloid cells (Fig. 4 C). In striking contrast to the dominant lymphoid potential of MPP4 cells in sham hosts, MPP4 cells in CL&P recipient mice generated a significant number of myeloid cells (Fig. 4 D), demonstrating that the microenvironment in the post-infection mice indeed drives differentiation of lymphoid-primed precursors to the myeloid lineage.

An infection-induced host factor, TIMP1, biases HSPC differentiation potential towards the myeloid lineage

During acute infection, proinflammatory cytokines, including IL-1, IL-6, G-CSF, and TNF, activate HSPCs to proliferate and generate more myeloid cells (Hormaechea-Agulla et al., 2020). However, these cytokines had returned to the preinfection baseline levels by 10 wk after CL&P surgery (Fig. 5 A), suggesting there must be other factors responsible for sustaining myeloid-biased hematopoiesis in mice after infection. We used a cytokine array to identify soluble factors that were elevated in CL&P mice compared with sham controls 10 wk after surgery. A striking difference between sham and CL&P samples was the presence of abundant TIMP1 in the latter (Fig. 5 A). Post-surgery kinetics analysis revealed that TIMP1 was produced at the highest level in the acute phase of infection, gradually decreased over time but still maintained at a higher level in CL&P mice relative to sham mice for at least 12 wk after surgery (Fig. 5 B). 12 wk after surgery, serum TIMP1 levels strongly correlated with granulocyte counts in the BM of sham and CL&P mice (Fig. 5 C).

We next investigated whether increased levels of TIMP1 in mice surviving severe infection played any role in myeloid-biased hematopoiesis. We cultured WT BM cells in methylcellulose medium with a suboptimal dose of cytokines and 10% serum from mice at 12 wk after sham or CL&P surgery. Significantly, more colonies were formed in the culture supplemented with serum from CL&P mice than with serum from sham mice (Fig. 5 D). Flow cytometry analyses showed an increased frequency of Ly6G+ granulocytes harvested from the CL&P serum culture compared with the sham control (Fig. 5 E), suggesting that soluble factors in CL&P serum stimulate myeloid differentiation. Treatment of cultures with an anti-TIMP1 antibody diminished the generation of Ly6G+ cells, indicating that TIMP1 is a cytokine in the CL&P serum that enhances myelopoiesis (Fig. 5, D and E). To explore the impact of TIMP1-upregulation on hematopoiesis in vivo, we transduced BM LSK cells with a

TIMP1-expressing retroviral vector and transferred these cells into irradiated *Timp1−/−* recipient mice. Overexpression of TIMP1 was only detected in mice reconstituted with TIMP1-expressing BM cells but not those received control viral vector–transduced BM cells (Fig. S4 A). Consistent with previous reports (Kobuch et al., 2015; Rossi et al., 2011), we found that TIMP1 deficiency did not affect myelopoiesis; however, overexpression of TIMP1 led to an expansion of CD11b+ myeloid cells (Fig. 5 F).

TIMP1 is produced by both myeloid and stromal cells (Boyd et al., 2020; Guccini et al., 2021; Kuroda et al., 2019; Wynn and Barron, 2010; Zhao et al., 2021). To determine the cellular contribution to the enhanced durable expression of TIMP1 after infection, we generated BM chimeras by transferring WT or *Timp1−/−* (KO) BM cells into irradiated CD45.1+ B6.SJL recipients and then performed sham or CL&P surgery 6 wk after BM engraftment (Fig. S4 B). Host mice receiving WT BM cells or KO BM cells manifested identical septic symptoms, and 50% WT and KO BM chimeras surviving sepsis had a comparable increase in granulocytes (Fig. S4 C). Of note, mice reconstituted with *Timp1−/−* BM cells had the same basal levels of TIMP1 after sham surgery and the same elevated amounts of TIMP1 after CL&P surgery as those seen in WT BM chimeras (Fig. S4 D), indicating that tissue stromal cells rather than hematopoietic cells are the main producers of TIMP1 in sepsis surviving mice. To examine cellular sources of TIMP1 within the BM compartment, we isolated CD45+ hematopoietic cells, CD45− CD31+ endothelial cells, and CD45− CD31− stromal cells from sham and CL&P mice (Fig. S4 E) and determined *Timp1* transcript levels by RT-PCR. In line with the aforementioned BM reconstitution experiments, CD45+ cells expressed little *Timp1* in both sham and CL&P mice. Endothelial cells expressed basal levels of *Timp1* which were not upregulated by infection. Of note, sham BM stromal cells contained 3.5 times higher *Timp1* transcripts than sham endothelial cells, and there was twofold upregulation of *Timp1* transcripts in CL&P BM stromal cells relative to the sham counterpart (Fig. 5 G). To further identify the cellular sources of TIMP1 at steady state, we examined published datasets of BM stromal cells (Dolgalev and Tikhonova, 2021). Our analysis revealed that fibroblasts, chondrocytes, and osteogenic cells contain TIMP1 producers (Fig. S4, F and G).

TIMP1 promotes myelopoiesis through inhibiting proteolytic activation of Notch in HSPCs

Since the main function of TIMP1 is to inhibit metalloproteinases, we hypothesized that TIMP1 may promote myelopoiesis through the regulation of metalloproteinases that are involved in HSC fate decision. ADAM10 appears to be a putative TIMP1 target since it is the essential sheddase activating Notch, which in turn governs lineage specification during hematopoiesis (Ng et al., 2021; Stier et al., 2002; Tian et al., 2008). To test this hypothesis, we first determined the potency of TIMP1 on
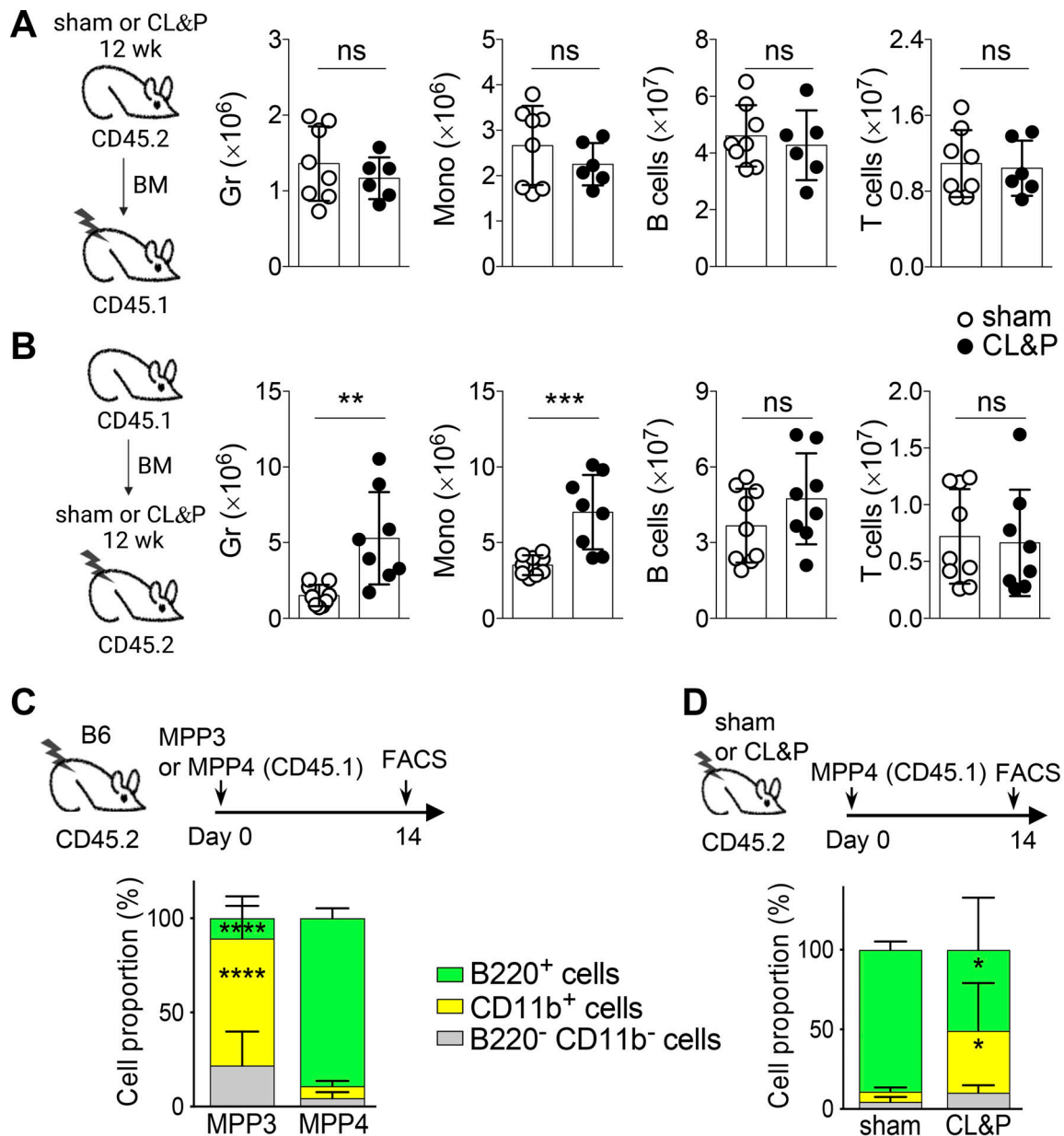
Figure 4. **The hematopoietic microenvironment of mice surviving sepsis enhances myeloid output. (A)** BM cells from B6 mice at 12 wk after sham or CL&P surgery were transferred into irradiated B6.SJL mice, respectively. 6 wk later, FACS analysis was performed to determine the total number of myeloid cells (Gr and Mono) and lymphocytes (B and T cells) in the spleen. Each symbol represents one mouse, with eight mice engrafted with sham donor cells and six mice with CL&P donor cells (data combined from two independent experiments). Bars show the mean value ± SD. ns, P > 0.05 (unpaired two-tailed Student's *t* test). **(B)** BM cells from B6.SJL mice were transferred into irradiated B6 mice at 12 wk after sham surgery (*n* = 9) or CL&P surgery (*n* = 8). 6 wk later, FACS analysis was performed to determine the total numbers of myeloid cells (Gr and Mono) and lymphocytes (B and T cells) in the spleen. Symbols represent each mouse and data were collected from two independent experiments. Bars represent the mean value ± SD. * P < 0.05; ns, P > 0.05 (unpaired two-tailed Student's *t* test). **(C)** MPP3 or MPP4 cells from B6.SJL mice were transferred into sublethally irradiated naïve B6 mice. 14 days later, FACS analysis was performed to determine the frequencies of donor derived CD45.1⁺ CD11b⁺ myeloid cells and CD45.1⁺ B cells in the peripheral blood. Data were collected from five recipient mice transplanted with MPP3 cells and six mice transplanted with MPP4 cells. Bars represent the mean value ± SD. **** P < 0.0001 (unpaired two-tailed Student's *t* test). **(D)** MPP4 cells from B6.SJL mice were transferred into sublethally irradiated sham (*n* = 6) or CL&P (*n* = 4) mice at 12 wk after surgery. 14 days later, FACS analysis was performed to determine the frequencies of donor-derived CD45.1⁺ CD11b⁺ myeloid cells and CD45.1⁺ B cells in the peripheral blood. Bars represent the mean value ± SD. * P < 0.05 (unpaired two-tailed Student's *t* test).

inhibiting ADAM10 proteolytic activity. Using an in vitro colorimetric assay, we found that TIMP1 inhibited ADAM10 activity as effectively as the ADAM10 inhibitor GI254023X (Fig. S5 A). To test whether TIMP1 was able to suppress Notch signaling, we measured the expression of the Notch target gene *Hes1* in

LSK cells stimulated with the Notch ligand DLL4. As expected, the expression of *Hes1* expression was reduced to baseline levels in LSK cells treated with the ADAM10 inhibitor due to a blockade of Notch activation in the absence of ADAM10 cleavage. In the presence of TIMP1, DLL4-stimulated LSK cells
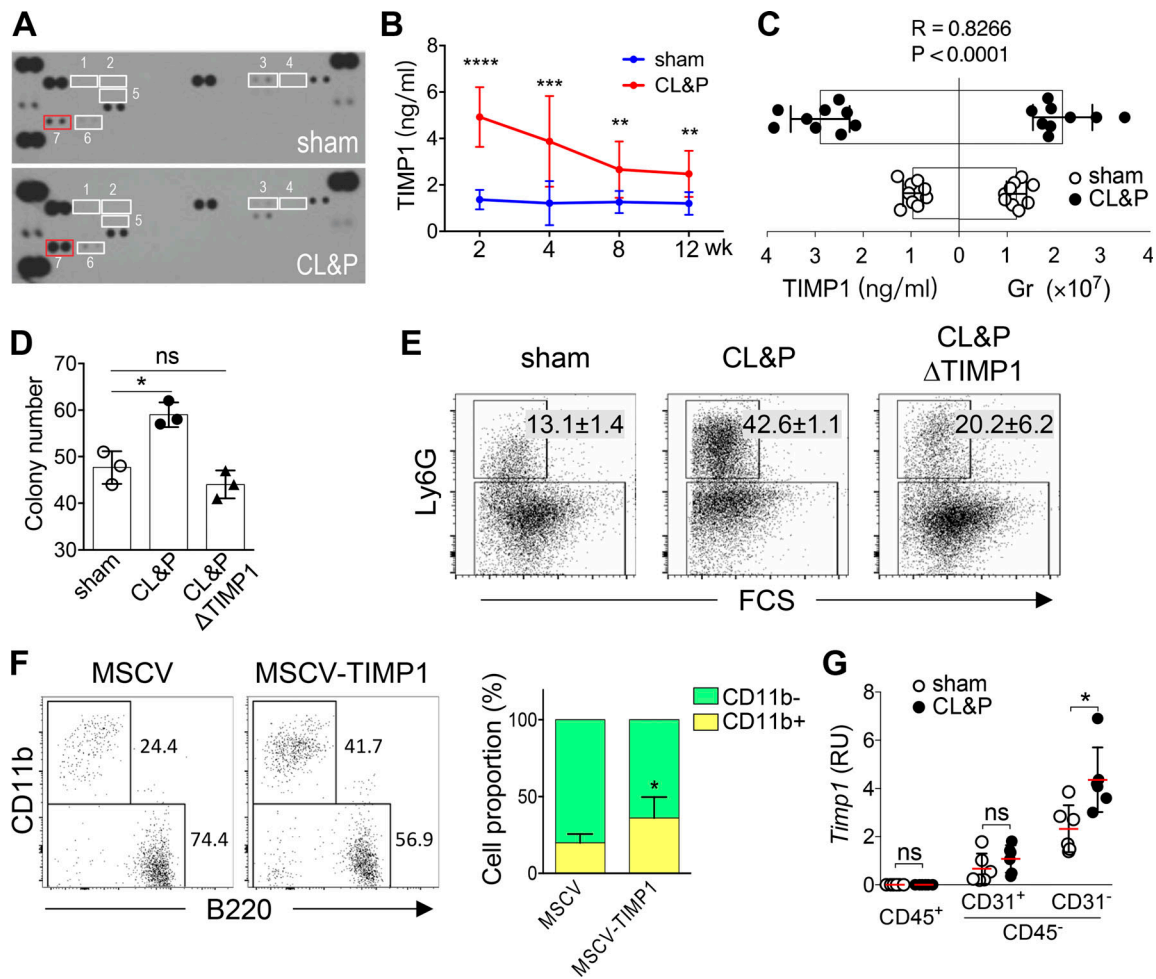
Figure 5. **Infection-induced TIMP1 in BM stromal cells enhances myeloid cell production. (A)** Cytokine array assay. Serum samples were pooled from three to five sham or CL&P mice at 10 wk after surgery. (1) G-CSF, (2) GM-CSF, (3) IL-1α, (4) IL-1β, (5) IL-6, (6) TNFα, (7) TIMP1. **(B)** ELISA measurement of circulating TIMP1 levels in mice at the indicated time points after sham surgery ($n = 10$) or CL&P surgery ($n = 14$). ** $P < 0.01$; *** $P < 0.001$; **** $P < 0.0001$. **(C)** Correlation between serum levels of TIMP1 and the number of BM granulocytes in mice at 12 wk after sham surgery ($n = 9$) or CL&P surgery ($n = 9$). Each symbol represents an individual mouse, and the data were pooled from three independent experiments. Bars represent the mean value ± SD. The Spearman correlation coefficient (R) and its associated P value (P) are indicated. **(D)** Numbers of colonies formed in the methylcellulose medium after a 10-day culture. The cultures were supplied with serum from sham or CL&P mice at 10 wk after surgery or with serum of CL&P mice plus anti-TIMP1 antibody. Symbols represent data of independent experiments with bars showing the mean value ± SD. * $P < 0.05$; ns, $P > 0.05$. **(E)** FACS analysis of cells collected from the culture described in Fig. 5 D. Percentages of Ly6G+ granulocytes are shown with the mean value ± SD. Data were collected from three independent cultures. **(F)** Representative FACS plots show the frequencies of CD11b+ and CD11b− cells in the peripheral blood of $Timp1^{-/-}$ host mice transferred with TIMP1-expressing BM cells or control BM cells. The right panel shows the percentages of CD11b+ cells. Data were collected from five mice/group. Bars represent the mean value ± SD. * $P < 0.05$. **(G)** qRT-PCR analysis of $Timp1$ transcripts in CD45+ cells, CD45−CD31+ endothelial cells and CD45−CD31− stromal cells purified from sham BM ($n = 6$) and CL&P BM ($n = 6$). Symbols represent data of individual mice compiled from two independent experiments, with the mean value ± SD. * $P < 0.05$; ns, $P > 0.05$ (unpaired two-tailed Student's t test). Source data are available for this figure: SourceData F5.

expressed as little *Hes1* as the ADAM10 inhibitor-treated cells (Fig. 6 A), indicating that TIMP1 efficiently inhibits Notch activation in LSK cells. Consistent with this in vitro observation, we found that *Hes1* expression was considerably lower in LSK cells from mice at week 12 after CL&P surgery compared with that from sham controls (Fig. 6 B). scRNA-seq analyses showed that while both sham and CL&P LSK cells expressed comparable levels of Notch receptors, ADAM10, γ-secretase complex subunits (Presenilin 1) and Notch co-activators (Mastermind-like [MAML], RBPJ) (Fig. S5 B), there were fewer CL&P LSK cells expressing Notch target genes and at much lower levels relative to sham LSK cells (Fig. 6 C). The gene sets of positive regulation

of Notch signaling were also found to be enriched in sham LSK cells as compared with CL&P LSK cells (Fig. S5 C). Together, these results indicate that while the expression of Notch signaling components is not altered in CL&P LSK cells, Notch signaling in these cells is suppressed by TIMP1-mediated inhibition of ADAM10 proteolytic activity.

To further determine whether inhibition of Notch signaling in LSK cells was relevant to the myeloid-biased HSPC differentiation, we cultured LSK cells from B6 mice with cytokines (SCF and Flt3L) that support LSK cell proliferation and myeloid differentiation (Varnum-Finney et al., 2011). Notch signaling activated by DLL4 significantly suppressed the development of
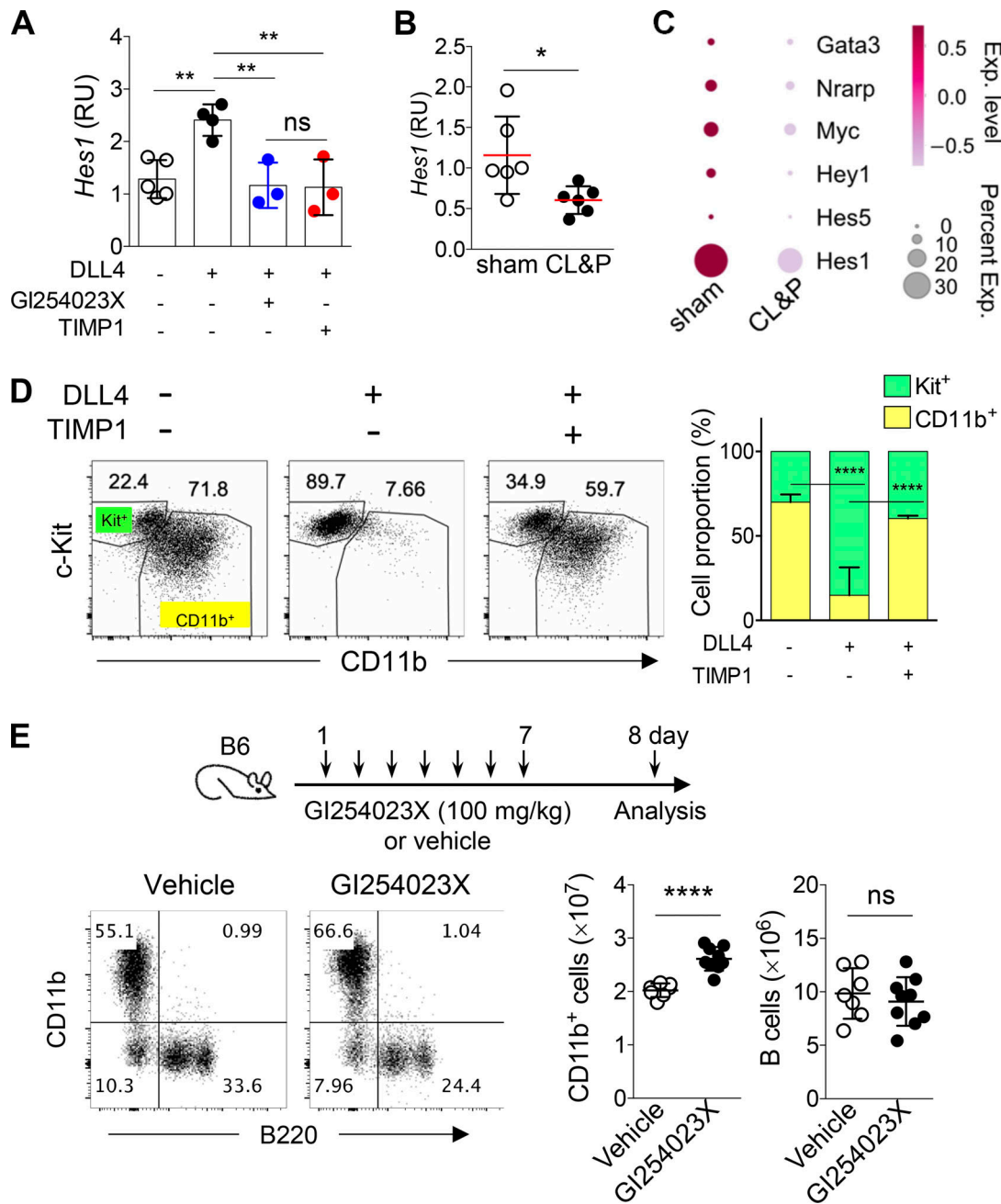
Figure 6. **TIMP1 inhibits Notch signaling-mediated suppression of myeloid differentiation. (A)** *Hes1* expression in DLL4 stimulated LSK cells in the culture. LSK cells purified from B6 mice were cultured in a medium with indicated stimuli for 5 h. Expression of *Hes1* transcripts was determined by qRT-PCR. Symbols depict data from three to five independent experiments with bars showing the mean value ± SD. ** P < 0.01; ns, P > 0.05 (unpaired two-tailed Student's *t* test). **(B)** Expression of *Hes1* transcripts in LSK cells sorted from mice at 12 wk after sham surgery (*n* = 6) or CL&P surgery (*n* = 6). Symbols represent individual mice; red lines show the mean value. * P < 0.05 (unpaired two-tailed Student's *t* test). **(C)** Dot plot presentation of Notch target gene expression in scRNA-seq datasets of sham or CL&P LSK cells. **(D)** TIMP1 antagonizes DLL4-mediated suppression of myelopoiesis in vitro. LSK cells sorted from B6 mice were cultured with DLL4 in the presence or absence of TIMP1. CD11b⁺ cells developed in the 5-day culture were analyzed by FACS and shown in dot plots. The right panel shows statistics from six independent cell cultures. Bars depict the mean value ± SD. **** P < 0.0001 (unpaired two-tailed Student's *t* test). **(E)** Treatment scheme and representative FACS plots showing percentages of CD11b⁺ myeloid cells and B cells in the BM of GI254023X-treated mice (*n* = 9) or vehicle-treated mice (*n* = 7). Statistic numbers of CD11b⁺ cells and B cells in the BM with the average cell counts ± SD are shown in the bottom right panel. Each dot represents an individual mouse. Data were compiled from two independent experiments. **** P < 0.0001; ns, P > 0.05 (unpaired two-tailed Student's *t* test).

CD11b⁺ myeloid cells in a 5-day culture, and the addition of TIMP1 in the culture antagonized the suppressive activity of DLL4 on myeloid differentiation (Fig. 6 D). Moreover, in vivo inhibition of ADAM10 by treating mice with GI254023X led to an increase in CD11b⁺ myeloid cells (Fig. 6 E). These findings thus demonstrate that high levels of TIMP1 can promote myelopoiesis through inhibition of the ADAM10-Notch signaling axis in mouse HSPCs.

TIMP1 is upregulated in human sepsis survivors and enhances myeloid differentiation of human HSPCs in vitro

To investigate whether TIMP1 has a relevant role in hematopoiesis in human sepsis, we determined the plasma levels of TIMP1 in sepsis patients and in healthy age-matched persons. Plasma samples were collected from patients at the time of sepsis diagnosis (n = 22) or from sepsis survivors at 6 mo after hospital discharge (n = 4). TIMP1 levels were 10-fold higher in the plasma of patients with sepsis than in healthy people (Fig. 7 A). A high mortality rate within the first 28 days of hospitalization was seen in patients with a high level of circulating TIMP1 (Fig. 7 B), indicating that TIMP1 levels correlate to the severity of sepsis. Furthermore, TIMP1 levels were approximately threefold higher in sepsis survivors 6 mo after hospital discharge compared with age-matched healthy controls (Fig. 7 C). Taken together, these findings indicate that, as observed in mouse sepsis model, severe infection in humans also induces rapid upregulation of TIMP1 expression, which is maintained at a higher level even after infection has resolved.

Next, we sought to determine whether TIMP1 also influenced human HSPC differentiation by regulating the Notch signaling pathway. Human HSPCs with >90% of CD45⁺ CD34⁺ cells were obtained from the BM of healthy donors (Table S4). Upon stimulation with DLL4, human CD34⁺ HSPCs significantly upregulated Hes1 expression, and the addition of either the ADAM10 inhibitor GI254023X or TIMP1 suppressed Hes1 expression (Fig. 7 D). To examine whether TIMP1 promoted myelopoiesis of human CD34⁺ HSPCs, we monitored CD11b⁺ myeloid cells developed from the cultured human HSPCs under different stimulation conditions. We found that activation of Notch signaling in HSPCs suppressed myeloid differentiation, as significantly less CD11b⁺ cells were generated in the culture in the presence of DLL4 (Fig. 7 E). The addition of TIMP1 in the culture reversed DLL4-mediated suppression of myelopoiesis in vitro (Fig. 7 E). Thus, these results demonstrate that, similar to what we observed in our mouse sepsis model, infection also induces TIMP1 upregulation in human sepsis patients, which is maintained for a long time after the infection is resolved. In addition, our data support the hypothesis that TIMP1 could also promote persistent post-infection myelopoiesis by suppressing Notch signaling in human HSPCs.

Discussion

Upon infection, HSCs rapidly shift from a homeostatic to an inflammatory state and increase the output of immune cells of mostly myeloid lineages to boost innate immunity (Baldridge et al., 2011; Caiado et al., 2021; Chavakis et al., 2019). Since a balanced production of multi-hematopoietic lineage cells is crucial to the immune system function, it is important to understand whether hematopoiesis could return to the pre-infection state, and if not, what is the mechanism that perturbs HSC function after severe infection. In this report, we used a mouse CL&P polymicrobial peritonitis (sepsis) model as a paradigm of hematopoiesis during and after severe infection. Data about hematopoiesis after sepsis are scanty, possibly due to an assumption that hematopoiesis returns to the steady state, since the proinflammatory cytokines known to influence hematopoiesis have decreased to the basal level. In contrast to this assumption, our results reveal that at least up to 3 mo after surgery, HSPCs have not returned to the preinfection homeostasis. There are still significantly more HSPCs in the cell cycle in CL&P mice as compared with that in sham mice. Unlike steady-state HSPCs that mainly rely on glycolysis (Ito and Suda, 2014; Takubo et al., 2013), CL&P HSPCs preferentially use mitochondrial biosynthesis and respiration metabolic pathways. Metabolic regulators such as Sirt7 and Foxo3, known to suppress myelopoiesis (Kaiser et al., 2020; Miyamoto et al., 2007; Mohrin et al., 2015), are downregulated in CL&P HSPCs as compared with sham HSPCs. Concordant with this molecular signature, CL&P HSPCs generate significantly more myeloid cells relative to sham HSPCs. Thus, emergency myelopoiesis induced by infection persists after the known proinflammatory cytokines wane and the infection has been cleared.

It has been reported that HSPCs not only sense and respond to but also remember the infection so that trained immunity can be acquired following infection as infection-experienced HSPCs preferentially produce more innate immune cells relative to naïve HSPCs (Bekkering et al., 2021). Microbial components, such as Candida albicans β-glucan and Bacillus Calmette–Guérin vaccine can induce HSPC-intrinsic metabolic and epigenetic alterations, thereby establishing an inflammatory memory in HSPCs after infection (Kaufmann et al., 2018; Mitroulis et al., 2018). In our experimental setting, we find that CL&P HSPCs function similarly to sham HSPCs after being transferred into a non-inflammatory environment. Importantly, naïve lymphoid-primed MMP4 cells without prior experience of inflammation began to produce a significantly high number of myeloid cells after being transferred into CL&P mice. Our results show that infection could upregulate novel mediators, such as TIMP1, that bias HSPC differential potential to sustain myeloid-biased hematopoiesis beyond the acute phase of severe infection. This mechanism is likely conserved in mice and humans, given our observation that TIMP1 is also upregulated in human patients surviving sepsis and that TIMP1 promotes myelopoiesis of human HSPCs in vitro. TIMP1 has been shown to be upregulated in BM stromal cells of aged mice, as well as by infection-mimicking agents, such as lipopolysaccharide and polyinosinic–polycytydilic acid (Helbling et al., 2019). Further studies are needed to elucidate whether TIMP1 exhibits a similar myeloid-boosting effect in milder infection conditions and inflammaging. It will also be important to determine whether TIMP1 can cooperate with somatic mutations associated with clonal hematopoiesis of indeterminate potential to further enhance myeloid-biased hematopoietic output.
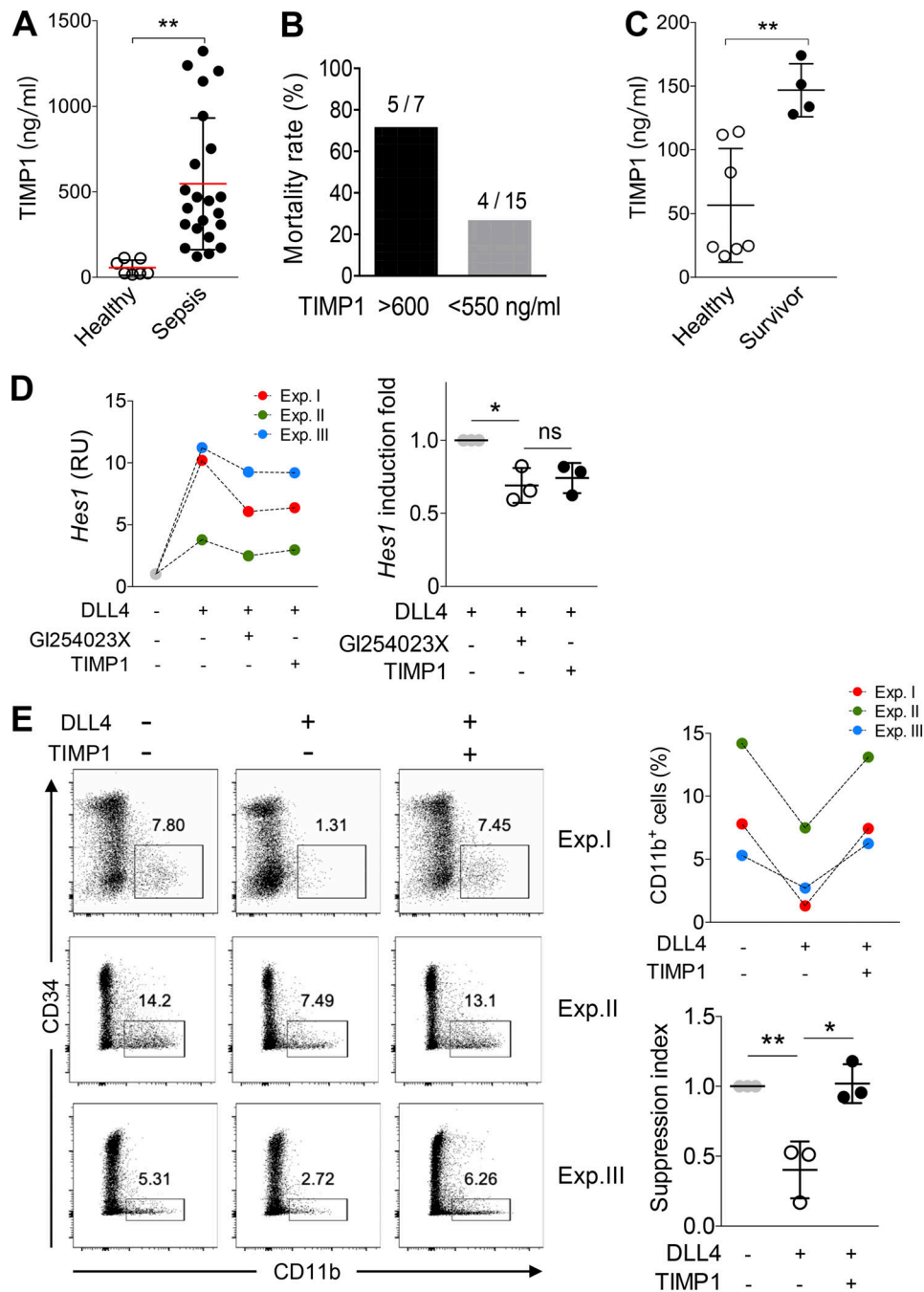
Figure 7. **TIMP1 is upregulated in human sepsis survivors and inhibits Notch-mediated suppression of myelopoiesis of cultured human HSPCs.** **(A)** Levels of circulating TIMP1 in age-matched healthy persons (*n* = 7) and in patients in ICU with sepsis (*n* = 22). Symbols indicate individual subjects; red lines show the mean value ± SD. ** P < 0.01 (unpaired two-tailed Student's *t* test). **(B)** Mortality rates of septic patients with circulating TIMP1 levels higher than 600 ng/ml or lower than 550 ng/ml. **(C)** Circulating TIMP1 levels in healthy individuals (*n* = 7) or in sepsis survivors (*n* = 4) at 6 mo after release from ICU. Symbols show data from individual persons with the mean value ± SD. ** P < 0.01 (unpaired two-tailed Student's *t* test). **(D)** *Hes1* expression in human HSPCs. Human CD34$^+$ HSPCs were cultured in medium with indicated stimuli for 5 h. Expression of *Hes1* transcripts was determined by qRT-PCR. Induction fold of *Hes1* is calculated as the ratio of *Hes1* levels stimulated with DLL4 plus GI254023X or TIMP1 to that with DLL4 alone. Symbols depict data from three independent experiments. * P < 0.05; ns, P > 0.05 (unpaired two-tailed Student's *t* test). RU, relative unit. **(E)** Cultured human HSPCs under the indicated conditions are FACS analyzed by the indicated markers. Percentages of CD11b$^+$ cells developed in the 5-day culture are given. The suppression index of myeloid differentiation is calculated as the ratio of the percentage of CD11b$^+$ cells generated with DLL4 ± TIMP1 to that without DLL4. Symbols depict data from three independent experiments. * P < 0.05; ** P < 0.01 (unpaired two-tailed Student's *t* test).

The BM hematopoietic niche contains various types of cells that foster and educate residing HSCs through cell–cell interactions and secreted mediators (Morrison and Scadden, 2014). Our studies show that infection induces BM stromal cells to produce excessive TIMP1. TIMP1 has not been considered a conventional proinflammatory factor, despite previous literature showing elevated circulating TIMP1 levels in patients with septic shock (Lorente et al., 2014), acute respiratory distress syndrome (Boyd et al., 2020), and inflammatory malignancy (Zhao et al., 2021). TIMP1 is also nonessential for steady-state hematopoiesis (Rossi et al., 2011); however, overexpression of TIMP1 enhances granulopoiesis (Kobuch et al., 2015). Mechanistically, our studies show that TIMP1 inhibits ADAM10-mediated proteolytic activation of Notch. Notch signaling has a complex role in adult hematopoiesis (Bigas and Espinosa, 2012; Lampreia et al., 2017). For example, deletion of *Rbpj*, the transcription factor of canonic Notch signaling, has no effect on hematopoiesis under both steady-state and stress conditions nor does it affect the expression of Notch target genes (Duarte et al., 2018). On the other hand, Notch signaling and its target *Hes1* have been shown to govern the HSC cell fate by suppressing the expression of myelomonocytic transcriptomes (Klinakis et al., 2011; Varnum-Finney et al., 2011). Defective Notch signaling leads to myeloproliferative disorder (Kim et al., 2008; Klinakis et al., 2011), which also phenocopies that of ADAM10 knockout mice (Yoda et al., 2011). Here, we have observed that the generation of myeloid cells is drastically inhibited when both mouse and human HSPCs are cultured in the presence of the Notch ligand DLL4 and that the addition of TIMP1 counteracts the inhibitory effects of DLL4. In agreement with the functional assays, our scRNA-seq analyses reveal that Notch target genes are downregulated in CL&P HSPCs relative to sham cells, which is accompanied by the expansion of an aberrant population of progenitor cells that co-expressed both myeloid and lymphoid commitment genes. These results thus support a model that under the steady state MPPs may commit to the lymphoid cell fate by upregulating the lymphoid transcriptomes and simultaneously downregulating the myelomonocytic transcriptomes by Notch signaling. However, in the post-infection host that overexpresses TIMP1, lymphoid cell-fate specified MPPs cannot complete the cell-fate determination because Notch signaling attenuated by TIMP1 is not sufficient to repress the myelomonocytic gene expression program, thus re-directing the cell fate toward the myeloid trajectory.

Taken together, our work shows that hematopoiesis has not returned to the homeostatic state even after severe infection has resolved. The persistent inflammatory state of HSPCs is supported by an altered hematopoietic microenvironment in animals surviving severe infection. Our studies identify TIMP1 as a previously undescribed inflammatory mediator that regulates HSPC differentiation toward the myeloid lineage via the ADAM10-Notch signaling axis. It is likely that simultaneous derangement of multiple pathways, rather than a single mediator, is involved in maintaining the inflammatory state of hematopoiesis after severe infection. Future studies are needed to identify other novel factors and the biological processes that contribute to enhanced myelopoiesis after infection.

Materials and methods
Human data
Plasma samples
Plasma samples were obtained from patients enrolled in a prospective, non-therapeutic study of adults 21 years of age or older who had a clinical diagnosis of sepsis with known or suspected infection and who were treated at North Shore University Hospital between March 14, 2008 and January 25, 2010. Sepsis was defined as the presence of any two of the following clinical features: core body temperature ≥38°C or ≤36°C, heart rate ≥ 90, respiratory rate ≥ 20, total ventilation >10 L/min or a $PaCo_2$ of <32 mmHg, WBC ≥ 12,000 or ≤ 4,000, or a differential count showing >10% bands. Patients were excluded from the study if they were pregnant or breast feeding, hospitalized <10 days prior to the current visit, had a history of BM or solid organ transplant, alcoholism, i.v. drug use, chemotherapy, or neutropenia. Plasma samples were obtained at the time of sepsis diagnosis and for a subset of the patients who survived sepsis, at 6 mo after hospital discharge. Blood was collected from sepsis patients with routine morning samples or from a central line access when available to decrease the need for additional needle sticks. As controls, blood was collected from healthy age-matched subjects. Blood processing: 1 ml of EDTA anti-coagulated blood from each study subject was processed for plasma by two rounds of centrifugation (1,000 rpm followed by 10,000 rpm) and then filtration through a 0.22-μm filter. Plasma samples were stored frozen at –70°C until used for analysis. All procedures were approved by The Feinstein Institutes for Medical Research/Northwell Health Office of the Institutional Review Board (IRB# 05-091). All study subjects provided informed written consent.

Human HSPCs
CD34+ HSPCs were purchased from StemCell Technologies and HemaCare, respectively (Table S4).

Mice
C57BL/6J (B6), B6.SJL-Ptprc^a Pepc^b/BoyJ (B6.SJL), and B6.129S4-Timp1^{tm1Pds}/J (Timp1^{−/−}) mice were purchased from the Jackson Laboratory. Mice were housed under specific pathogen–free conditions. Rodent chow and water were provided ad libitum. Mice were at the age of 8–12 wk when experiments started. Animal experiments were approved by the Institutional Animal Care and Use Committee of the Feinstein Institutes of Medical Research and were performed in accordance with the institutional, state, and federal guidelines.

Sepsis induction
CL&P was performed to induce sepsis in accordance with an established protocol (Cuenca et al., 2010). 8-wk-old male mice were anesthetized with 3% isoflurane and with O_2 flow at 1 L/min. A midline incision was made at the abdomen to exteriorize the cecum. Approximately, one-third of the cecum from its distal end was ligated using 3-0 polydioxanone (PDS II) sutures (Ethicon). The ligated cecum was then punctured once with a 22-gauge needle (BD Biosciences) and a small amount of feces (about 1 mm³) was extruded. After replacing the cecum into the

abdominal cavity, the abdominal wall was closed with 4-0 PDS II sutures (Ethicon) followed by a skin closure with medical surgical clips (Braintree Scientific). Sham mice underwent the same surgery except for the ligation and puncture of the cecum. All mice were resuscitated by subcutaneous injection of 1 ml of PBS supplemented with antibiotics (imipenem/cilastatin, 0.5 mg/kg body weight).

Retroviral vector construction and viral infection

Mouse *Timp1* cDNA was obtained by PCR with *Timp1*-specific primers and cloned into the retroviral expressing vector MSCV-GFP to generate the MSCV-TIMP1 construct. Retrovirus was produced by calcium phosphate transfection of 293FT cells (Invitrogen) with MSCV-TIMP1 and a helper plasmid pCL-Eco. Retroviral supernatants were collected twice at 36 and 60 h after transfection.

BM cells were harvested at day 5 after mice received i.p. injection of 3 mg/kg 5-flurouracil (5-FU; Sigma-Aldrich) and cultured in DMEM supplemented with 10% FCS (Hyclone), 10 ng/ml IL-3 (PeproTech), 10 ng/ml IL-6 (PeproTech), and 50 ng/ml SCF (PeproTech). Retroviral infection of BM cells was achieved by spin infection using retroviral supernatants according to a standard protocol.

Transplantations

For MPP cell transplantation, sham and CL&P mice (12 wk after surgery) were sublethally irradiated (7 Gy) and i.v. injected 3,000 MPP3 or MPP4 cells sorted from B6.SJL mice.

All recipient mice in the following BM reconstitution experiments received a total of 10 Gy irradiation delivered in two split doses with a 3-h interval.

For the reciprocal reconstitution studies, 2×10^6 total BM cells collected from B6 mice (CD45.2$^+$) at 12 wk after sham or CL&P surgery were i.v. injected into B6.SJL recipients (CD45.1$^+$), respectively. Reciprocally, 2×10^6 BM cells were collected from B6.SJL mice (CD45.1$^+$) and i.v. injected into irradiated B6 mice (CD45.2$^+$) at 12 wk after sham or CL&P surgery.

For transplantation of TIMP1-overexpressing HSCs, 2×10^5 retroviral transduced BM cells were transplanted into irradiated *Timp1$^{-/-}$* mice.

To assess whether TIMP1 was derived from hematopoietic or stromal cells, 2×10^6 total BM cells from *Timp1$^{-/-}$* mice or WT littermates were i.v. injected into irradiated B6.SJL recipients (CD45.1$^+$) to generate the BM chimeras.

ADAM10 inhibitor treatment

The ADAM10 inhibitor GI254023X (MedChemExpress) was dissolved in 0.1 M carbonate buffer containing 20% DMSO at 10 mg/ml. 10- to 12-wk-old B6 mice were treated with GI254023X via daily i.p. injection at a dose of 100 mg/kg body weight for 7 days. Control mice received an identical volume of vehicle following the same administration scheme.

Flow cytometry and cell sorting

Splenocytes or BM cells from two pairs of tibias and femurs per mouse were harvested and red blood cells were lysed using ACK (ammonium-chloride-potassium) lysing buffer (150 mM NH$_4$Cl,

10 mM KHCO$_3$, 0.1 mM EDTA). Cells were resuspended in FACS buffer (PBS supplemented with 2 mM EDTA and 0.5% BSA), stained for different cell surface markers, and then subjected to flow cytometric analysis or cell sorting.

For isolation of stromal cells, tibias and femurs were dissected and cleaned to remove attached tissues and then cut into ~1-mm^3 pieces with scissors in digestion buffer (DMEM supplemented with 2% FBS [Gibco], 10 mM HEPES [Lonza], 1 mg/ml Collagenase P [#11249002001; Roche], 1 mg/ml Dispase II [#4942078001; Roche] and 66 μg/ml DNase I [Sigma-Aldrich]). Samples were incubated in a 37°C oven with constant rotation for 15 min. Cell suspensions were removed and fresh digestion buffer was added to the remaining bone fragments for an additional 15 min digestion. Cells from the two-step digestions were combined and red blood cells were lysed with ACK lysing buffer.

Flow cytometric analysis was performed on an LSR II or a Fortessa flow cytometer (BD Biosciences) and analyzed with FlowJo software (v.10.0; TreeStar). All antibodies used are listed in Table S5. To analyze cell populations in the spleen, B220, TCR, CD11b, and Gr1 were used to detect B and T lymphocytes, monocytes, and granulocytes, respectively. To examine the BM cell compartment, a cocktail containing antibodies for lineage markers (Lin) was used: B220, CD19, TCR, CD3, CD4, CD8, CD11c, CD11b, Gr1, Ly6C, F4/80, TER119, and NK1.1 (clone PK136). Other antibodies specific to the following markers were also used for the study: c-Kit, Sca1, CD34, CD150, CD48, and Flt3. Gating definition for HSPCs were as follows: LSK, Lin$^-$Sca1$^+$c-Kit$^+$; LT-HSC, CD150$^+$CD48$^-$CD34^{low}Flt3$^-$ LSK; ST-HSC, CD150$^-$CD48$^-$CD34^{hi}Flt3$^-$ LSK; MPP2, CD150$^+$CD48$^+$Flt3$^-$ LSK; MPP3, CD150$^-$CD48$^+$Flt3$^-$ LSK; and MPP4, CD150$^-$CD48$^+$Flt3$^+$ LSK. To analyze human HSPC differentiation in vitro, we used anti-human CD34 and anti-human CD11b antibodies.

For cell cycle analysis, following staining for LSK cell surface markers, cells were fixed and permeabilized with BD Cytofix/Cytoperm buffer (BD Biosciences). Intracellular staining for Ki67 was done using PermWash solution (BD Biosciences). DAPI (Sigma-Aldrich) was then added for DNA content determination.

Cell sorting was performed on a FACSAria II instrument (BD Biosciences). Lin$^-$ cells were enriched from BM cells prior to sorting using EasySep Mouse Hematopoietic Progenitor Cell Isolation Kit (StemCell Technologies). Lin$^-$ enriched cells were then stained with antibodies specific for Lin, c-Kit, and Sca1 for sorting LSK cells. To sort BM endothelial cells and stromal cells, as well as CD45$^+$ hematopoietic cells, enzyme-digested cells were separated into Lin$^-$ and Lin$^+$ populations using EasySep Mouse Hematopoietic Progenitor Cell Isolation Kit (StemCell Technologies). CD45$^+$ cells were sorted by staining Lin$^+$ cells with anti-CD45. Lin$^-$ cells were stained with anti-CD45, anti-TER119, anti-CD71, and anti-CD31. Endothelial cells were sorted as CD45$^-$ TER119$^-$ CD71$^-$ CD31$^+$ and stromal cells were sorted as CD45$^-$ TER119$^-$ CD71$^-$ CD31$^-$ cells.

In vitro HSPC cultures

For activation of Notch signaling, the Notch ligand DLL4 (5 μg/ml of human or mouse DLL4 [R&D]) was coated to U-bottom

wells (high-binding 96-well plate; Greiner Bio-One) that had been pretreated with RetroNectin (Takara) following the manufacturer's instruction. 24 h later, wells were washed with PBS, and human or mouse HSPCs were added to the wells and cultured at 37°C for 5 h to induce Notch activation.

LSK cells were sorted from the BM of B6 mice. To determine the expression of the Notch target gene *Hes1* by RT-PCR, 2×10^4 LSK cells were seeded into DLL4-coated wells in DMEM supplemented with 10% FCS (Hyclone), 10 ng/ml SCF (PeproTech), and 2 ng/ml Flt3L (PeproTech) in the presence or absence of 100 ng/ml mouse TIMP1 (R&D) or 1 μM GI254023X (R&D) for 5 h. To examine HSPC differentiation, 4,000–10,000 LSK cells per well were cultured in a previously described medium (DMEM with 10% FCS [Hyclone], 50 ng/ml SCF [PeproTech], and 100 ng/ml Flt3L [PeproTech]) (Varnum-Finney et al., 2011) in the presence or absence of 100 ng/ml of mouse TIMP1 for 5 days.

Human HSPCs (Table S4) were cultured in StemSpan SFEM II medium with StemSpan CD34+ Expansion Supplement (StemCell Technologies). To determine the expression of human *Hes1* by RT-PCR, human HSPCs were seeded into DLL4-precoated wells at 2×10^4 cells/well and cultured for 5 h ±100 ng/ml of human TIMP1 (R&D) or 1 μM GI254023X (R&D). To examine HSPC differentiation, 5×10^3–10^4 human HSPCs were cultured with plate-bound DLL4 with or without 100 ng/ml of human TIMP1 (R&D) for 5 days before being subjected to FACS analysis.

For colony formation assays, a suboptimal conditioned methylcellulose medium was made by mixing M3434 (StemCell Technologies) with M3134 (StemCell Technologies) at a ratio of 1:10. Serum pooled from five mice at 10 wk after sham or CL&P surgery were added to the suboptimal condition to a final concentration of 10%. In some experiments, CL&P serum was pretreated with anti-TIMP1 antibody. BM cells from B6 mice were plated at 2×10^4 cells/3 ml/plate in 35-mm Petri dishes in the suboptimal conditioned methylcellulose medium with sham or CL&P serum. After a 10-day culture, colonies in each plate were counted and cells were then harvested for flow cytometric analysis.

Immunoassays

For examination of cytokines in the serum of sham and CL&P mice, serum samples collected from five mice at 10 wk after sham or CL&P surgery were pooled, respectively. Cytokines were detected using Proteome Profiler Mouse Cytokine Array Panel A according to the manufacturer's instructions (R&D).

For measurement of circulating TIMP1 levels, mouse serum was collected at indicated time points and human samples were obtained from septic patients and septic survivors. The amounts of TIMP1 were measured using a mouse or human TIMP1 Quantikine ELISA Kit according to the manufacturer's instructions (R&D).

For evaluation of the inhibitory activity of TIMP1 on ADAM10, a colorimetric assay was performed to determine ADAM10-mediated cleavage of a fluorogenic peptide substrate Mca-PLAQAV-Dpa-RSSSR-NH2 (R&D) in the presence or absence of TIMP1.

38 μM of recombinant mouse ADAM10 (R&D) was mixed with 20 μM of Mca-PLAQAV-Dpa-RSSSR-NH2 with or without 45 μM recombinant mouse TIMP1 (BioLegend) or 1 μM of the ADAM10 inhibitor GI 254023X (R&D). The reactions were incubated at 37°C for 30 min, and the amount of cleaved peptide substrate was measured by OD_{405} using a Synergy H1 Hybrid reader (BioTek) and was calculated as the relative unit of ADAM10 proteolytic activity.

Quantitative real-time PCR (qRT-PCR)

Total RNAs were isolated from FACS sorted or cultured cells using RNeasy Micro Kit (for cells $<10^5$) or RNeasy Mini Kit (QIAGEN) and reverse-transcribed into cDNA using a SuperScript III cDNA Synthesis Kit (Invitrogen) according to the manufacturers' instructions. qRT-PCR using cDNA, gene-specific primers, and SYBR Green Master Mix (Thermo Fisher Scientific) was performed on a LightCycler 480 II instrument (Roche). Relative expression was quantified using the ΔΔ Ct methods and normalized to *Actb*.

Gene-specific primers are as follows:

Mouse *Timp1*: Forward 5′-CTGGCATCTGGCATCCTCTTG-3′ and Reverse 5′-GTGGTCTCGTTGATTTCTGG-3′;
Mouse *Hes1*: Forward 5′-TCCAAGCTAGAGAAGGCAGAC-3′ and Reverse 5′-TGATCTGGGTCATGCAGTTG-3′;
Mouse *Actb*: Forward 5′-GCTCTTTTCCAGCCTTCCTTC-3′ and Reverse 5′-CTCCTTCTGCATCCTGTCAG-3′;
Human *Hes1*: Forward 5′-TTGGATGCTCTGAAGAAAG-3′ and Reverse 5′-TTCTCCAGCTTGGAATG-3′;
Human *Actb*: Forward 5′-AAGGCCAACCGCGAGAAGATG-3′ and Reverse 5′-ATCACGATGCCAGTGGTAC-3′.

scRNA-seq and analysis

LSK cells were sorted from three mice at 12 wk after sham and CL&P surgery, respectively. Cells were washed and resuspended in PBS containing 0.04% BSA at 800 cells/μl for the targeted recovery of 10,000 cells. Single-cell partitioning and cDNA library construction were done using Chromium Single Cell 3′ Kit v3 per the manufacturer's instruction (10X Genomics). Library sequencing was performed using NovaSeq S4 (Illumina) at Yale Center for Genome Analysis.

Cell Ranger (10X Genomics) was used to process raw sequencing data. For the sham sample, the mean reads per cell was 115,132 and the median genes per cell was 2,881. For CL&P sample, the mean reads per cell was 98,713 and the median genes per cell was 3,202. Subsequent data filtering, normalization, and PC analysis (PCA) were conducted with PartekFlow (Partek). Cells that passed the following criteria were used for further analysis: (1) the percentage of mitochondrial genes per cell ≤10%; (2) the percentage of ribosome genes per cell was between 25% and 50%; and (3) the number of detected genes is between 700 and 5,500. Cells that passed the quality control (88%) were then filtered by lineage-associated marker genes (Table S1), resulting in an LSK cell dataset containing 3,021 sham cells and 3,843 CL&P cells. The data were $\log_2$ transformed and normalized. After PCA, the first 20 PCs were selected for the UMAP dimension reduction and clustering using the SLM modularity-

based clustering algorithm. The seven unsupervised clusters were annotated by reference-based classification using previously published datasets (Pei et al., 2020; Rodriguez-Fraticelli et al., 2020). Trajectory analysis with Monocle 3, GO, and gene set enrichment analyses was carried out on the platform of PartekFlow (Partek).

Statistical analysis

All statistics were performed using Prism software (version 6; GraphPad). Two-tailed Student's t tests were used, with P values <0.05 considered to be statistically significant.

Online supplemental material

Fig. S1 shows the mortality rate caused by CL&P surgery, the hematopoietic changes in the periphery following CL&P surgery, and the gating strategy of HSPCs. Fig. S2 provides the procedure for scRNA-seq and the classification of HSPC cell clusters. Fig. S3 shows additional scRNA-seq data for changed biological processes in the post-infection HSPCs. Fig. S4 shows the gating strategy for BM stromal cells and the BM cellular sources of TIMP1. Fig. S5 shows the inhibition of ADAM10 cleavage activity by TIMP1 and Notch signaling in the post-infection HSPCs. Table S1 contains lineage-associated marker genes used to filter contaminated cells in scRNA-seq data sets. Table S2 lists top expressed genes of LT-HSCs and MPPs. Table S3 contains a list of core signature genes of the five trajectory leaf nodes. Table S4 lists the sources and information of human HSPCs used in this study. Table S5 contains a list of antibodies and reagents used for flow cytometry analysis.

Data availability

The scRNA-seq dataset is available in the Gene Expression Omnibus database under accession number GSE205728. This study also uses a published dataset under accession number GSE145491 (Klein et al., 2022) and data from "Study: Resolving the bone marrow niche heterogeneity" (https://singlecell.broadinstitute.org/single_cell/study/SCP1248).

Acknowledgments

We thank Pinguang Yang and HaoTing Yen for technical assistance. Some figures were created using BioRender.com.

Author contributions: T. Song designed and performed research, analyzed data, and contributed to writing; Y. Yao performed experiments; J. Papoin and L. Blanc helped with scRNA-seq experiments; B. Sherry and B. Diamond provided critical reagents; H. Gu interpreted data and edited the manuscript; L. Blanc contributed to writing; Y. Zou conceived and designed the study, supervised research, interpreted data, and wrote the manuscript.

References

Baccin, C., J. Al-Sabah, L. Velten, P.M. Helbling, F. Grünschläger, P. Hernández-Malmierca, C. Nombela-Arrieta, L.M. Steinmetz, A. Trumpp, and S. Haas. 2020. Combined single-cell and spatial transcriptomics reveal the molecular, cellular and spatial bone marrow niche organization. Nat. Cell Biol. 22:38–48. https://doi.org/10.1038/s41556-019-0439-6

Baldridge, M.T., K.Y. King, and M.A. Goodell. 2011. Inflammatory signals regulate hematopoietic stem cells. Trends Immunol. 32:57–65. https://doi.org/10.1016/j.it.2010.12.003

Baryawno, N., D. Przybylski, M.S. Kowalczyk, Y. Kfoury, N. Severe, K. Gustafsson, K.D. Kokkaliaris, F. Mercier, M. Tabaka, M. Hofree, et al. 2019. A cellular taxonomy of the bone marrow stroma in homeostasis and leukemia. Cell. 177:1915–1932.e16. https://doi.org/10.1016/j.cell.2019.04.040

Batsivari, A., M.L.R. Haltalli, D. Passaro, C. Pospori, C. Lo Celso, and D. Bonnet. 2020. Dynamic responses of the haematopoietic stem cell niche to diverse stresses. Nat. Cell Biol. 22:7–17. https://doi.org/10.1038/s41556-019-0444-9

Bekkering, S., J. Domínguez-Andrés, L.A.B. Joosten, N.P. Riksen, and M.G. Netea. 2021. Trained immunity: Reprogramming innate immunity in health and disease. Annu. Rev. Immunol. 39:667–693. https://doi.org/10.1146/annurev-immunol-102119-073855

Bigas, A., and L. Espinosa. 2012. Hematopoietic stem cells: To be or Notch to be. Blood. 119:3226–3235. https://doi.org/10.1182/blood-2011-10-355826

Boyd, D.F., E.K. Allen, A.G. Randolph, X.Z.J. Guo, Y. Weng, C.J. Sanders, R. Bajracharya, N.K. Lee, C.S. Guy, P. Vogel, et al. 2020. Exuberant fibroblast activity compromises lung function via ADAMTS4. Nature. 587:466–471. https://doi.org/10.1038/s41586-020-2877-5

Caiado, F., E.M. Pietras, and M.G. Manz. 2021. Inflammation as a regulator of hematopoietic stem cell function in disease, aging, and clonal selection. J. Exp. Med. 218:e20201541. https://doi.org/10.1084/jem.20201541

Chavakis, T., I. Mitroulis, and G. Hajishengallis. 2019. Hematopoietic progenitor cells as integrative hubs for adaptation to and fine-tuning of inflammation. Nat. Immunol. 20:802–811. https://doi.org/10.1038/s41590-019-0402-5

Chen, C., Y. Liu, R. Liu, T. Ikenoue, K.L. Guan, Y. Liu, and P. Zheng. 2008. TSC-mTOR maintains quiescence and function of hematopoietic stem cells by repressing mitochondrial biogenesis and reactive oxygen species. J. Exp. Med. 205:2397–2408. https://doi.org/10.1084/jem.20081297

Ciarlo, E., T. Heinonen, C. Théroude, F. Asgari, D. Le Roy, M.G. Netea, and T. Roger. 2020. Trained immunity confers broad-spectrum protection against bacterial infections. J. Infect. Dis. 222:1869–1881. https://doi.org/10.1093/infdis/jiz692

Cuenca, A.G., M.J. Delano, K.M. Kelly-Scumpia, L.L. Moldawer, and P.A. Efron. 2010. Cecal ligation and puncture. Curr. Protoc. Immunol. Chapter 19:Unit 19 13. https://doi.org/10.1002/0471142735.im1913s91

Dolgalev, I., and A.N. Tikhonova. 2021. Connecting the dots: Resolving the bone marrow niche heterogeneity. Front. Cell Dev. Biol. 9:622519. https://doi.org/10.3389/fcell.2021.622519

Duarte, S., P.S. Woll, N. Buza-Vidas, D.W.L. Chin, H. Boukarabila, T.C. Luís, L. Stenson, T. Bouriez-Jones, H. Ferry, A.J. Mead, et al. 2018. Canonical Notch signaling is dispensable for adult steady-state and stress myelo-erythropoiesis. Blood. 131:1712–1719. https://doi.org/10.1182/blood-2017-06-788505

Fink, M.P. 2014. Animal models of sepsis. Virulence. 5:143–153. https://doi.org/10.4161/viru.26083

Guccini, I., A. Revandkar, M. D'Ambrosio, M. Colucci, E. Pasquini, S. Mosole, M. Troiani, D. Brina, R. Sheibani-Tezerji, A.R. Elia, et al. 2021. Senescence reprogramming by TIMP1 deficiency promotes prostate cancer metastasis. Cancer Cell. 39:68–82.e9. https://doi.org/10.1016/j.ccell.2020.10.012

Helbling, P.M., E. Piñeiro-Yáñez, R. Gerosa, S. Boettcher, F. Al-Shahrour, M.G. Manz, and C. Nombela-Arrieta. 2019. Global transcriptomic

profiling of the bone marrow stromal microenvironment during post-natal development, aging, and inflammation. *Cell Rep.* 29:3313–3330.e4. https://doi.org/10.1016/j.celrep.2019.11.004

Hormaechea-Agulla, D., D.T. Le, and K.Y. King. 2020. Common sources of inflammation and their impact on hematopoietic stem cell biology. *Curr. Stem Cell Rep.* 6:96–107. https://doi.org/10.1007/s40778-020-00177-z

Hotchkiss, R.S., G. Monneret, and D. Payen. 2013. Sepsis-induced immuno-suppression: From cellular dysfunctions to immunotherapy. *Nat. Rev. Immunol.* 13:862–874. https://doi.org/10.1038/nri3552

Ishibashi, T., T. Yokota, Y. Satoh, M. Ichii, T. Sudo, Y. Doi, T. Ueda, Y. Nagate, Y. Hamanaka, A. Tanimura, et al. 2018. Identification of MS4A3 as a reliable marker for early myeloid differentiation in human hemato-poiesis. *Biochem. Biophys. Res. Commun.* 495:2338–2343. https://doi.org/10.1016/j.bbrc.2017.12.117

Ito, K., M. Bonora, and K. Ito. 2019. Metabolism as master of hematopoietic stem cell fate. *Int. J. Hematol.* 109:18–27. https://doi.org/10.1007/s12185-018-2534-z

Ito, K., and T. Suda. 2014. Metabolic requirements for the maintenance of self-renewing stem cells. *Nat. Rev. Mol. Cell Biol.* 15:243–256. https://doi.org/10.1038/nrm3772

Kaiser, A., M. Schmidt, O. Huber, J.J. Frietsch, S. Scholl, F.H. Heidel, A. Hochhaus, J.P. Müller, and T. Ernst. 2020. SIRT7: An influence factor in healthy aging and the development of age-dependent myeloid stem-cell disorders. *Leukemia.* 34:2206–2216. https://doi.org/10.1038/s41375-020-0803-3

Kaufmann, E., J. Sanz, J.L. Dunn, N. Khan, L.E. Mendonça, A. Pacis, F. Tze-lepis, E. Pernet, A. Dumaine, J.C. Grenier, et al. 2018. BCG educates hematopoietic stem cells to generate protective innate immunity against tuberculosis. *Cell.* 172:176–190.e19. https://doi.org/10.1016/j.cell.2017.12.031

Kim, Y.W., B.K. Koo, H.W. Jeong, M.J. Yoon, R. Song, J. Shin, D.C. Jeong, S.H. Kim, and Y.Y. Kong. 2008. Defective Notch activation in microenvi-ronment leads to myeloproliferative disease. *Blood.* 112:4628–4638. https://doi.org/10.1182/blood-2008-03-148999

Klein, F., J. Roux, G. Cvijetic, P.F. Rodrigues, L. von Muenchow, R. Lubin, P. Pelczar, S. Yona, P. Tsapogas, and R. Tussiwand. 2022. Dntt expression reveals developmental hierarchy and lineage specification of hemato-poietic progenitors. *Nat. Immunol.* 23:505–517. https://doi.org/10.1038/s41590-022-01167-5

Klinakis, A., C. Lobry, O. Abdel-Wahab, P. Oh, H. Haeno, S. Buonamici, I. van De Walle, S. Cathelin, T. Trimarchi, E. Araldi, et al. 2011. A novel tumour-suppressor function for the Notch pathway in myeloid leu-kaemia. *Nature.* 473:230–233. https://doi.org/10.1038/nature09999

Kobuch, J., H. Cui, B. Grünwald, P. Saftig, P.A. Knolle, and A. Krüger. 2015. TIMP-1 signaling via CD63 triggers granulopoiesis and neutrophilia in mice. *Haematologica.* 100:1005–1013. https://doi.org/10.3324/haematol.2014.121590

Kuroda, N., M. Masuya, I. Tawara, J. Tsuboi, M. Yoneda, K. Nishikawa, Y. Kageyama, K. Hachiya, K. Ohishi, H. Miwa, et al. 2019. Infiltrating CCR2⁺ monocytes and their progenies, fibrocytes, contribute to colon fibrosis by inhibiting collagen degradation through the production of TIMP-1. *Sci. Rep.* 9:8568. https://doi.org/10.1038/s41598-019-45012-6

Lampreia, F.P., J.G. Carmelo, and F. Anjos-Afonso. 2017. Notch signaling in the regulation of hematopoietic stem cell. *Curr. Stem Cell Rep.* 3: 202–209. https://doi.org/10.1007/s40778-017-0090-8

Liu, Z., Y. Gu, S. Chakarov, C. Bleriot, I. Kwok, X. Chen, A. Shin, W. Huang, R.J. Dress, C.A. Dutertre, et al. 2019. Fate mapping via ms4a3-expression history traces monocyte-derived cells. *Cell.* 178:1509–1525.e19. https://doi.org/10.1016/j.cell.2019.08.009

Lorente, L., M.M. Martín, J. Solé-Violán, J. Blanquer, L. Labarta, C. Díaz, J.M. Borreguero-León, J. Orbe, J.A. Rodríguez, A. Jiménez, and J.A. Páramo. 2014. Association of sepsis-related mortality with early increase of TIMP-1/MMP-9 ratio. *PLoS One.* 9:e94318. https://doi.org/10.1371/journal.pone.0094318

Maneta, E., E. Aivalioti, S. Tual-Chalot, B. Emini Veseli, A. Gatsiou, K. Sta-matelopoulos, and K. Stellos. 2023. Endothelial dysfunction and im-munothrombosis in sepsis. *Front. Immunol.* 14:1144229. https://doi.org/10.3389/fimmu.2023.1144229

Mitroulis, I., K. Ruppova, B. Wang, L.S. Chen, M. Grzybek, T. Grinenko, A. Eugster, M. Troullinaki, A. Palladini, I. Kourtzelis, et al. 2018. Modulation of myelopoiesis progenitors is an integral component of trained immu-nity. *Cell.* 172:147–161.e12. https://doi.org/10.1016/j.cell.2017.11.034

Miyamoto, K., K.Y. Araki, K. Naka, F. Arai, K. Takubo, S. Yamazaki, S. Matsuoka, T. Miyamoto, K. Ito, M. Ohmura, et al. 2007. Foxo3a is essential for maintenance of the hematopoietic stem cell pool. *Cell Stem Cell.* 1:101–112. https://doi.org/10.1016/j.stem.2007.02.001

Mohrin, M., J. Shin, Y. Liu, K. Brown, H. Luo, Y. Xi, C.M. Haynes, and D. Chen. 2015. Stem cell aging. A mitochondrial UPR-mediated metabolic checkpoint regulates hematopoietic stem cell aging. *Science.* 347: 1374–1377. https://doi.org/10.1126/science.aaa2361

Moorlag, S.J.C.F.M., N. Khan, B. Novakovic, E. Kaufmann, T. Jansen, R. van Crevel, M. Divangahi, and M.G. Netea. 2020. β-Glucan induces pro-tective trained immunity against *Mycobacterium tuberculosis* infection: A key role for IL-1. *Cell Rep.* 31:107634. https://doi.org/10.1016/j.celrep.2020.107634

Morrison, S.J., and D.T. Scadden. 2014. The bone marrow niche for haematopoietic stem cells. *Nature.* 505:327–334. https://doi.org/10.1038/nature12984

Nakamura-Ishizu, A., K. Ito, and T. Suda. 2020. Hematopoietic stem cell metabolism during development and aging. *Dev. Cell.* 54:239–255. https://doi.org/10.1016/j.devcel.2020.06.029

Ng, H.L., E. Quail, M.N. Cruickshank, and D. Ulgiati. 2021. To Be, or Notch to Be: Mediating cell fate from embryogenesis to lymphopoiesis. *Bio-molecules.* 11:849. https://doi.org/10.3390/biom11060849

Niu, H., G. Fang, Y. Tang, L. Xie, H. Yang, L. Morel, B. Diamond, and Y.R. Zou. 2013. The function of hematopoietic stem cells is altered by both genetic and inflammatory factors in lupus mice. *Blood.* 121:1986–1994. https://doi.org/10.1182/blood-2012-05-433755

Pang, W.W., E.A. Price, D. Sahoo, I. Beerman, W.J. Maloney, D.J. Rossi, S.L. Schrier, and I.L. Weissman. 2011. Human bone marrow hematopoietic stem cells are increased in frequency and myeloid-biased with age. *Proc. Natl. Acad. Sci. USA.* 108:20012–20017. https://doi.org/10.1073/pnas.1116110108

Pei, W., F. Shang, X. Wang, A.K. Fanti, A. Greco, K. Busch, K. Klapproth, Q. Zhang, C. Quedenau, S. Sauer, et al. 2020. Resolving fates and single-cell transcriptomes of hematopoietic stem cell clones by PolyloxExpress barcoding. *Cell Stem Cell.* 27:383–395.e8. https://doi.org/10.1016/j.stem.2020.07.018

Pietras, E.M., D. Reynaud, Y.A. Kang, D. Carlin, F.J. Calero-Nieto, A.D. Leavitt, J.M. Stuart, B. Göttgens, and E. Passegué. 2015. Functionally distinct subsets of lineage-biased multipotent progenitors control blood pro-duction in normal and regenerative conditions. *Cell Stem Cell.* 17:35–46. https://doi.org/10.1016/j.stem.2015.05.003

Rodriguez-Fraticelli, A.E., C. Weinreb, S.W. Wang, R.P. Migueles, M. Jan-kovic, M. Usart, A.M. Klein, S. Lowell, and F.D. Camargo. 2020. Single-cell lineage tracing unveils a role for TCF15 in haematopoiesis. *Nature.* 583:585–589. https://doi.org/10.1038/s41586-020-2503-6

Rodriguez-Fraticelli, A.E., S.L. Wolock, C.S. Weinreb, R. Panero, S.H. Patel, M. Jankovic, J. Sun, R.A. Calogero, A.M. Klein, and F.D. Camargo. 2018. Clonal analysis of lineage fate in native haematopoiesis. *Nature.* 553: 212–216. https://doi.org/10.1038/nature25168

Rossi, L., A.V. Ergen, and M.A. Goodell. 2011. TIMP-1 deficiency subverts cell-cycle dynamics in murine long-term HSCs. *Blood.* 117:6479–6488. https://doi.org/10.1182/blood-2009-10-248955

Satoh, Y., T. Yokota, T. Sudo, M. Kondo, A. Lai, P.W. Kincade, T. Kouro, R. Iida, K. Kokame, T. Miyata, et al. 2013. The Satb1 protein directs he-matopoietic stem cell differentiation toward lymphoid lineages. *Im-munity.* 38:1105–1115. https://doi.org/10.1016/j.immuni.2013.05.014

Schultze, J.L., E. Mass, and A. Schlitzer. 2019. Emerging principles in mye-lopoiesis at homeostasis and during infection and inflammation. *Im-munity.* 50:288–301. https://doi.org/10.1016/j.immuni.2019.01.019

Stier, S., T. Cheng, D. Dombkowski, N. Carlesso, and D.T. Scadden. 2002. Notch1 activation increases hematopoietic stem cell self-renewal in vivo and favors lymphoid over myeloid lineage outcome. *Blood.* 99: 2369–2378. https://doi.org/10.1182/blood.v99.7.2369

Sudo, K., H. Ema, Y. Morita, and H. Nakauchi. 2000. Age-associated char-acteristics of murine hematopoietic stem cells. *J. Exp. Med.* 192: 1273–1280. https://doi.org/10.1084/jem.192.9.1273

Takizawa, H., S. Boettcher, and M.G. Manz. 2012. Demand-adapted regulation of early hematopoiesis in infection and inflammation. *Blood.* 119: 2991–3002. https://doi.org/10.1182/blood-2011-12-380113

Takubo, K., G. Nagamatsu, C.I. Kobayashi, A. Nakamura-Ishizu, H. Kobaya-shi, E. Ikeda, N. Goda, Y. Rahimi, R.S. Johnson, T. Soga, et al. 2013. Regulation of glycolysis by Pdk functions as a metabolic checkpoint for cell cycle quiescence in hematopoietic stem cells. *Cell Stem Cell.* 12:49–61. https://doi.org/10.1016/j.stem.2012.10.011

Terashima, A., K. Okamoto, T. Nakashima, S. Akira, K. Ikuta, and H. Takayanagi. 2016. Sepsis-induced osteoblast ablation causes

immunodeficiency. *Immunity*. 44:1434–1443. https://doi.org/10.1016/j.immuni.2016.05.012

Tian, L., X. Wu, C. Chi, M. Han, T. Xu, and Y. Zhuang. 2008. ADAM10 is essential for proteolytic activation of Notch during thymocyte development. *Int. Immunol.* 20:1181–1187. https://doi.org/10.1093/intimm/dxn076

Tikhonova, A.N., I. Dolgalev, H. Hu, K.K. Sivaraj, E. Hoxha, Á. Cuesta-Domínguez, S. Pinho, I. Akhmetzyanova, J. Gao, M. Witkowski, et al. 2019. The bone marrow microenvironment at single-cell resolution. *Nature*. 569:222–228. https://doi.org/10.1038/s41586-019-1104-8

van der Poll, T., M. Shankar-Hari, and W.J. Wiersinga. 2021. The immunology of sepsis. *Immunity*. 54:2450–2464. https://doi.org/10.1016/j.immuni.2021.10.012

Trumpp, A., M. Essers, and A. Wilson. 2010. Awakening dormant haematopoietic stem cells. *Nat. Rev. Immunol.* 10:201–209. https://doi.org/10.1038/nri2726

Vannini, N., M. Girotra, O. Naveiras, G. Nikitin, V. Campos, S. Giger, A. Roch, J. Auwerx, and M.P. Lutolf. 2016. Specification of haematopoietic stem cell fate via modulation of mitochondrial activity. *Nat. Commun.* 7:13125. https://doi.org/10.1038/ncomms13125

Varnum-Finney, B., L.M. Halasz, M. Sun, T. Gridley, F. Radtke, and I.D. Bernstein. 2011. Notch2 governs the rate of generation of mouse long- and short-term repopulating stem cells. *J. Clin. Invest.* 121:1207–1216. https://doi.org/10.1172/JCI43868

Wichterman, K.A., A.E. Baue, and I.H. Chaudry. 1980. Sepsis and septic shock--a review of laboratory models and a proposal. *J. Surg. Res.* 29:189–201. https://doi.org/10.1016/0022-4804(80)90037-2

Wynn, T.A., and L. Barron. 2010. Macrophages: Master regulators of inflammation and fibrosis. *Semin. Liver Dis.* 30:245–257. https://doi.org/10.1055/s-0030-1255354

Yoda, M., T. Kimura, T. Tohmonda, S. Uchikawa, T. Koba, J. Takito, H. Morioka, M. Matsumoto, D.C. Link, K. Chiba, et al. 2011. Dual functions of cell-autonomous and non-cell-autonomous ADAM10 activity in granulopoiesis. *Blood*. 118:6939–6942. https://doi.org/10.1182/blood-2011-06-357210

Zhao, L., A.D. Giannou, Y. Xu, A.M. Shiri, I. Liebold, B. Steglich, T. Bedke, T. Zhang, J. Lücke, P. Scognamiglio, et al. 2021. Efferocytosis fuels malignant pleural effusion through TIMP1. *Sci. Adv.* 7:eabd6734. https://doi.org/10.1126/sciadv.abd6734
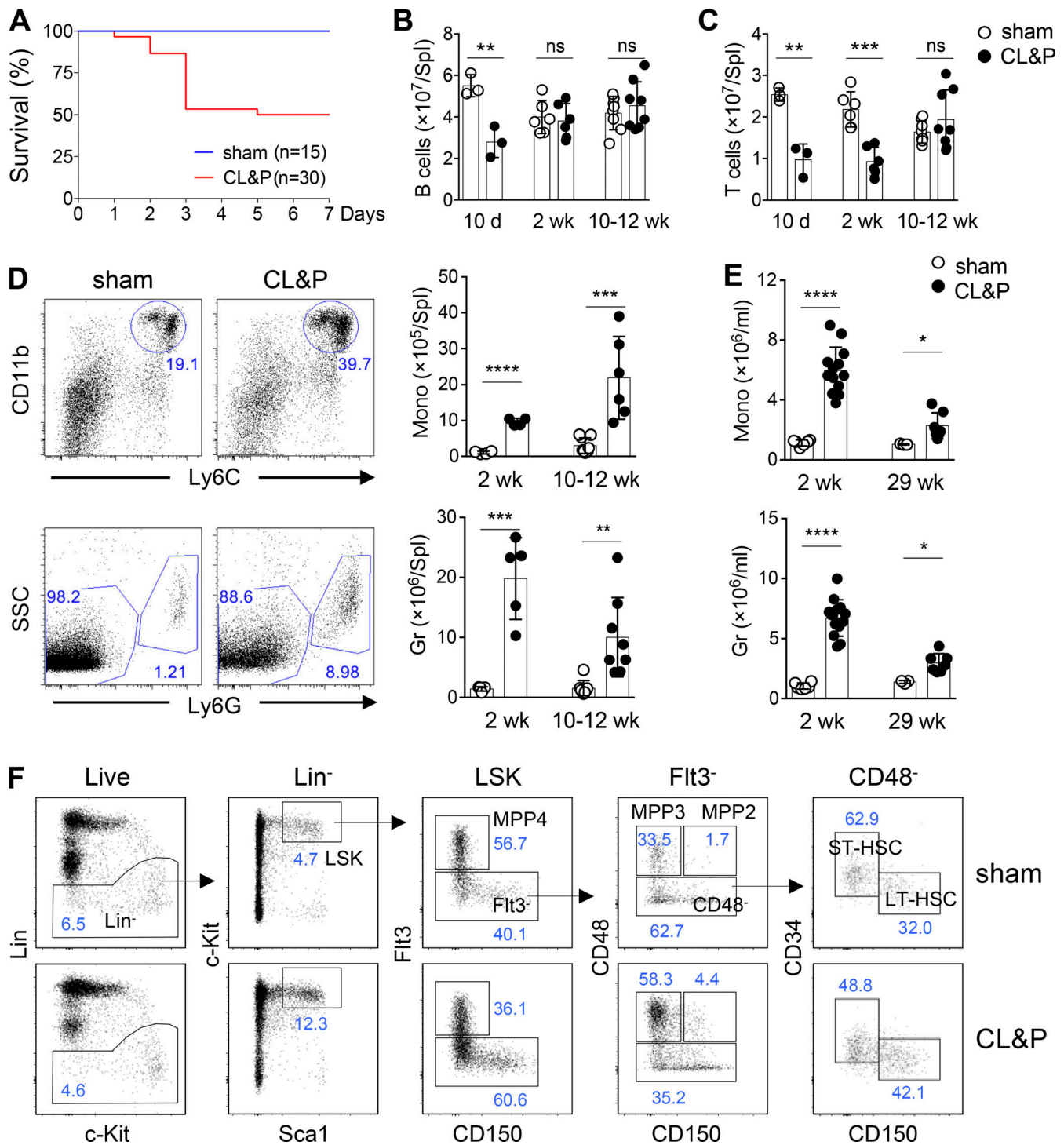
Supplemental material

Figure S1. **Changes in the hematopoietic compartments in mice at different time points after sham or CL&P surgery.** Related to Fig. 1. **(A)** Kaplan–Meier survival curves of sham and CL&P mice. Data were from three independent experiments. **(B)** The total number of splenic B cells in mice at the indicated time points after surgery (10 days: $n = 3$/group; 2 wk: $n = 6$/group; 10–12 wk: $n = 8$/group). Symbols represent data of individual mice collected from two experiments. Bars depict the mean value ± SD. ** P < 0.01; ns, P > 0.05 (unpaired two-tailed Student's t test). **(C)** The total number of splenic T cells in mice at different time points after surgery as indicated in B. Symbols represent data from individual mice; bars depict the mean value ± SD. ** P < 0.01; *** P < 0.001; ns, P > 0.05 (unpaired two-tailed Student's t test). **(D)** The left panel shows representative FACS plots depicting percentages of $CD11b^+Ly6C^+$ monocytes (Mono) or $Ly6G^+$ granulocytes (Gr) in the spleen of mice at week 12 after surgery. The right panel shows the statistics of the total number of monocytes and granulocytes. Symbols show the total numbers of monocytes or granulocytes in individual mice ($n = 4$–8); bars depict the mean value ± SD. ** P < 0.01; *** P < 0.001; **** P < 0.0001 (unpaired two-tailed Student's t test). **(E)** Symbols represent the total number of circulating monocytes or granulocytes in the blood of individual mice 2 wk after surgery (sham = 6, CL&P = 13) or 29 wk after surgery (sham = 3, CL&P = 7). Bars depict the mean value ± SD. * P < 0.05; **** P < 0.0001 (unpaired two-tailed Student's t test). **(F)** Gating strategy for LSK, LT-HSC, ST-HSC, MPP2, MPP3, and MPP4 cells. Representative plots are shown for sham and CL&P mice. Percentages of HSPC subsets were indicated.
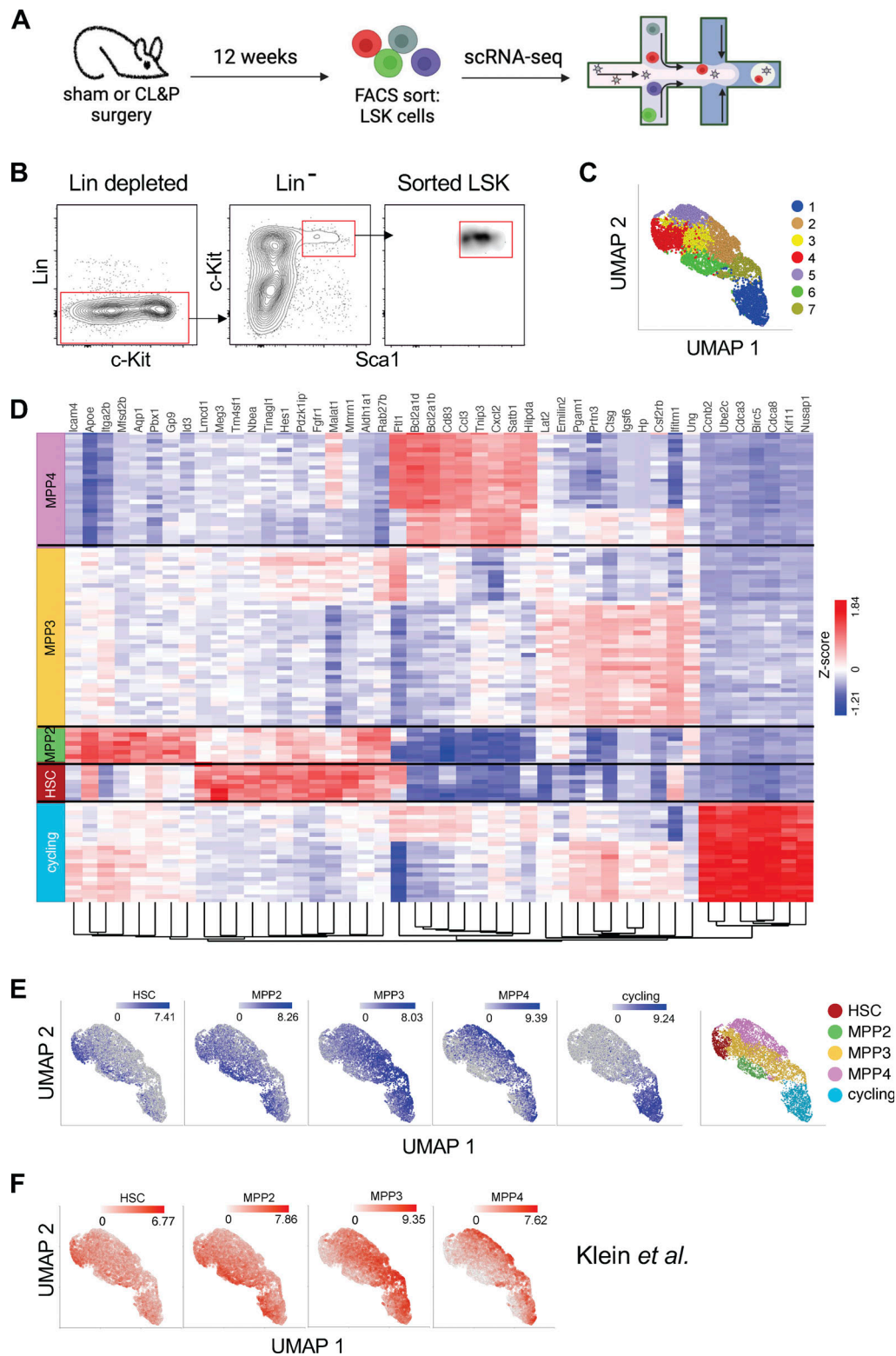
Figure. S2. **scRNA-seq analysis of LSK cells from sham and CL&P mice.** Related to Fig. 2. **(A)** Experimental procedure for scRNA-seq analysis. B6 mice were operated by sham or CL&P surgery. 12 wk later, BM cells were harvested from three sham and three CL&P mice, respectively, and LSK cells were sorted for scRNA-seq. **(B)** Gating strategy for FACS sorting LSK cells. **(C)** Unsupervised clustering of LSK cells visualized by a UMAP plot of merged sham and CL&P datasets. **(D)** Heatmap of expression of the top DEGs per cell state (row) in each cell (column). Expression of each gene was Z score transformed across the cells displayed in the heatmap. Dendrogram indicates the result of hierarchical clustering on genes expressed in the heatmap. **(E)** UMAP projection of scaled expression of gene signatures distinguishing HSCs, MPP2, MPP3, MPP4, and cycling cells. At right, a UMAP plot of merged sham and CL&P datasets shows cell-state clustering of LSK cells based on the expression of HSC and MPP signature genes. **(F)** UMAP projection of scaled expression of published gene signatures of HSCs, MPP2, MPP3, and MPP4 cells (Klein et al., 2022).
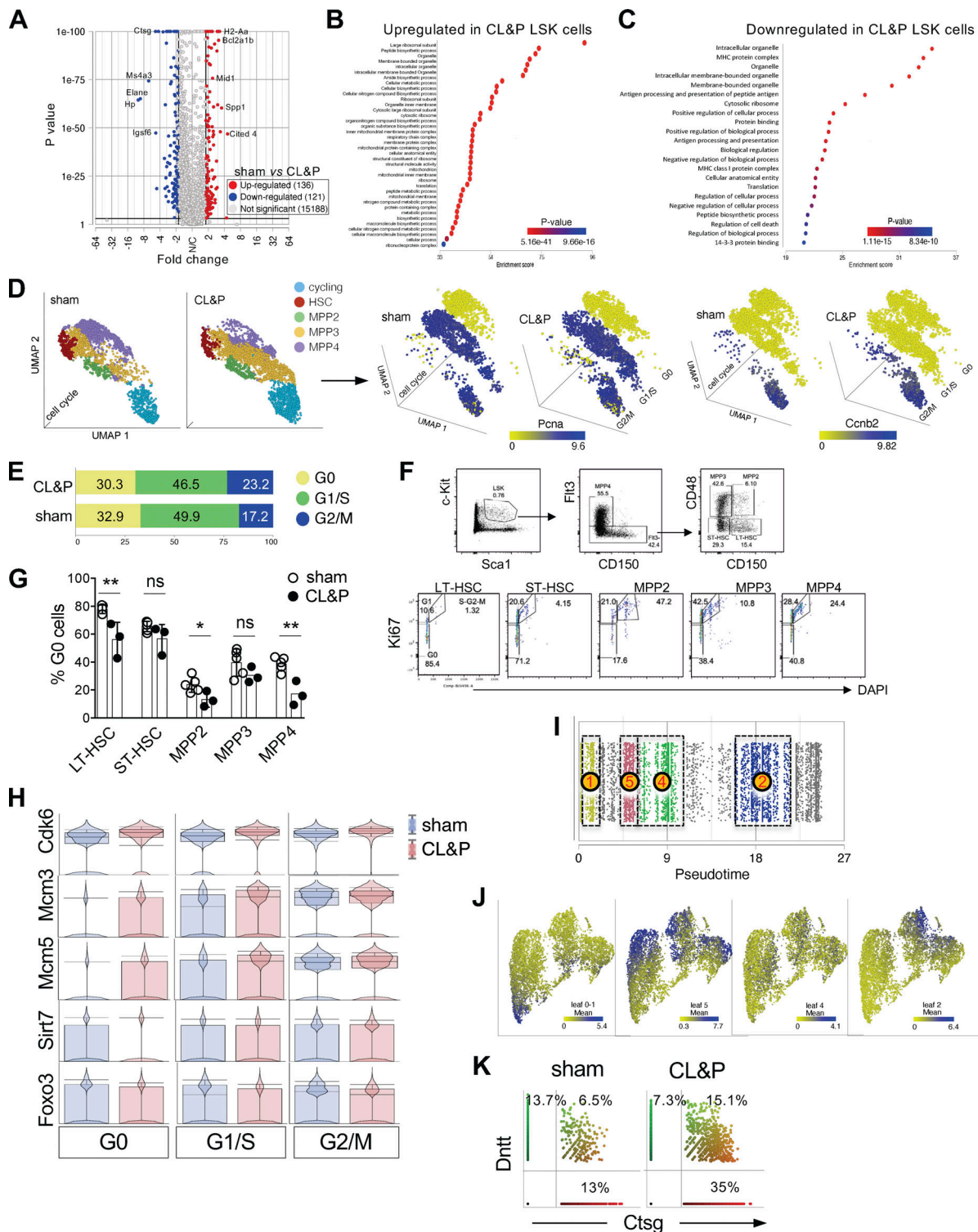
Figure S3. **Identification of transcriptomes associated with altered biological processes in LSK cells after infection.** Related to Fig. 3. **(A)** Volcano plot shows differentially expressed transcripts (1.8-fold change threshold, FDR < 0.05) upregulated in sham cells (red) or in CL&P cells (blue). **(B)** Biological process– and pathway–associated genes upregulated in CL&P cells. **(C)** Biological processes and pathway-associated genes downregulated in CL&P cells. **(D)** UMAP projection of the cell cycle phases of sham and CL&P LSK cells shown by expression of *Pcna* and *Ccnb2*. **(E)** Proportions of sham and CL&P LSK cells in each cell cycle phase. **(F)** Representative plots display the gating of HSPC subsets and measurement of proliferation via Ki67 expression and DNA content. **(G)** Percentages of HSCs and MPP cells in the G0 phase of the cell cycle are shown, with symbols depicting data of individual mice (sham = 5, CL&P = 3) and bars showing the mean value ± SD. *P < 0.05; ** P < 0.01; ns, P > 0.05 (unpaired two-tailed Student's *t* test). **(H)** Violin plots of transcript expression values for the indicated genes in sham and CL&P LSK cells in the indicated cell cycle phases. **(I)** Specification of the trajectory leaf nodes on the pseudotime domains of merged sham and CL&P datasets. **(J)** Trajectory UMAP projection of scaled expression of core signatures of each leaf node of merged sham and CL&P datasets. **(K)** Scatterplots display co-expression of the lymphoid-specific gene *Dntt* and the myeloid-specific gene *Ctsg*.
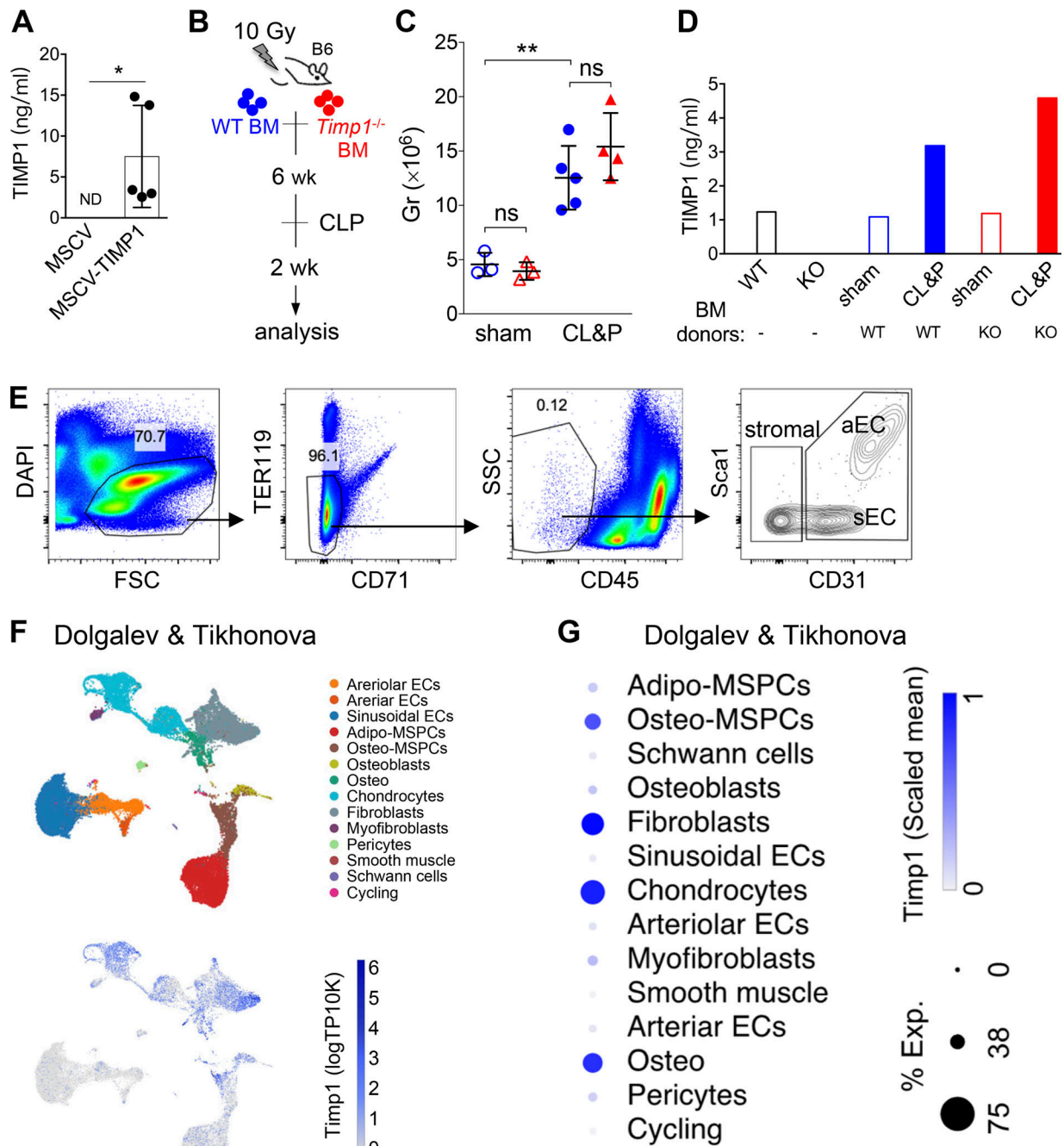
Figure S4. **Identification of TIMP1 as an infection-induced host factor.** Related to Fig. 5. **(A)** Serum levels of TIMP1 in *Timp1^{-/-}* recipient mice reconstituted with BM cells infected with a retroviral vector expressing TIMP1 (MSCV-TIMP1) or a control vector (MSCV). Each group contains five mice. Symbols represent individual mice. * P < 0.05 (unpaired two-tailed Student's *t* test). **(B)** Experimental procedure. **(C)** Total granulocytes in the BM of recipient mice at 2 wk after surgery. Symbols represent individual mice. ** P < 0.01; ns, P > 0.05 (unpaired two-tailed Student's *t* test). **(D)** ELISA measurement of TIMP1 levels in the serum samples pooled from five WT or *Timp1^{-/-}* mice, as well as from five recipient mice engrafted with WT BM cells or *Timp1^{-/-}* BM cells (*n* = 5). **(E)** Sorting strategy for purifying BM CD45⁻CD31⁺ endothelial cells (including both sinusoidal [sEC] and arteriolar endothelial cells [aEC]) and CD45⁻CD31⁻ stromal cells. **(F)** The top UMAP plot highlights the BM stromal cell clusters, and the bottom UMAP depicts *Timp1* expression levels. **(G)** Dot-plot presentation of *Timp1* expression in the published scRNA-seq datasets (Dolgalev and Tikhonova, 2021).
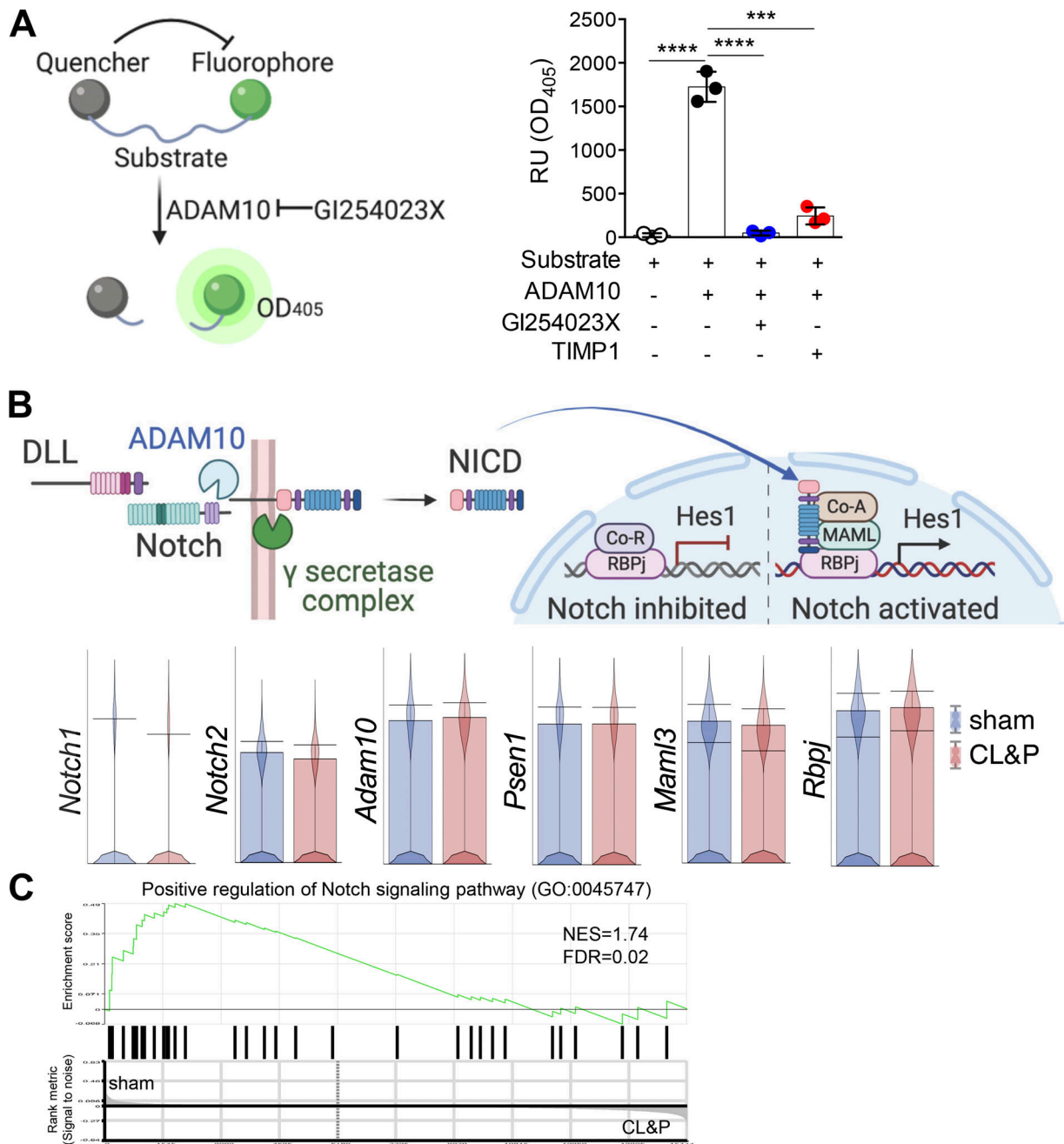
Figure S5. **TIMP1 inhibits ADAM10 proteolytic activity and Notch signaling in sham and CL&P LSK cells.** Related to Fig. 6. **(A)** Schematic outline of the colorimetric assay. Proteolytic activity of ADAM10 in the presence or absence of inhibitor GI254023X or TIMP1 was measured by a colorimetric assay. Symbols depict data from three independent experiments with bars showing the mean value ± SD. **** $P < 0.0001$; *** $P < 0.001$ (unpaired two-tailed Student's *t* test). **(B)** Top panel shows proteolytic activation of Notch signaling. Bottom violin plots show the equal expression of Notch receptors, Notch sheddases, and Notch co-activators in sham and CL&P LSK cells. **(C)** GSEA of the Notch signaling pathway gene signature in sham versus CL&P LSK cells.

Provided online are Table S1, Table S2, Table S3, Table S4, and Table S5. Table S1 contains lineage-associated marker genes used to filter contaminated cells in scRNA-seq data sets. Table S2 lists the top expressed genes of LT-HSCs and MPPs. Table S3 contains a list of core signature genes of the five trajectory leaf nodes. Table S4 lists the sources and information of human HSPCs used in this study. Table S5 contains a list of antibodies and reagents used for flow cytometry analysis.